A new method to derive water vapor supersaturation at cumulus cloud base from in situ measurements

Ramon C. Braga[1], Manfred Wendisch[2], Rachel Albrecht[3], Daniel Harrison[1,4]

[1] Reefs and Oceans Research Cluster, National Marine Science Centre, Southern Cross University, Coffs Harbour, Australia.
[2] Leipzig Institute for Meteorology, Leipzig University, Leipzig, Germany.
[3] Instituto de Astronomia, Geofísica e Ciências Atmosféricas, Universidade de São Paulo, São Paulo, Brazil.
[4] School of Geosciences, University of Sydney, Sydney, Australia

Correspondence to: Ramon C. Braga (ramon.braga@scu.edu.au)

Abstract. Current in situ measurements of water vapor supersaturation (S_v) with respect to liquid water at cloud base are highly uncertain due to instrumental limitations. Consequently, S_v is commonly estimated using cloud microphysical models and parameterizations. Here, we derive S_v at warm cumulus cloud base from in situ measurements through calculations of the energy and water vapor budgets associated with cloud formation. The derived S_v provides a thermodynamic analogue to the supersaturation established in a cloud condensation nuclei (CCN) chamber, enabling direct comparison with independently measured CCN activation spectra below cloud base. To this end, we formulate the energy budget of a saturated rising air parcel at cloud base and treat the transition between saturated thermodynamic states locally as quasi-isobaric. Under these conditions, the latent heat (Q) released during condensational droplet growth is determined by the corresponding sensible enthalpy difference between the saturated-vapor and water vapor-liquid states. According to the first law of thermodynamics, Q is partitioned between the change in internal energy (ΔU) and water vapor expansion work (W_s). Within this diagnostic framework, part of the condensational energy is, therefore, spent on W_s, reducing the amount of liquid water formed relative to the limiting case in which the entire condensational energy contributes to droplet growth. Accordingly, the cloud supersaturation (S_c) is diagnostically partitioned into liquid-phase (S_l) and vapor-phase (S_v) components based on the fractions of Q associated with ΔU and W_s, respectively. This framework enables the derivation of S_v from airborne cloud-base measurements through thermodynamic constraints on condensational energy partitioning. Here we use airborne measurements collected in growing convective cumuli over the Amazon Basin during the ACRIDICON-CHUVA campaign. Our results demonstrate that the derived cloud droplet number concentration as a function of S_v agrees, within measurement uncertainties, with S_v activation spectra of CCN measured below cloud base.

1 Introduction

A realistic representation of cloud formation processes and their impact on the atmospheric energy budget and water cycle is crucial for accurate numerical weather prediction and reliable climate projection models (IPCC, 2021). Liquid water cloud droplets form in a rising humid (i.e., water vapor containing) air parcel, which expands during ascent due to decreasing air pressure. The expansion causes a cooling of the air parcel until the relative humidity (RH) exceeds 100 %. In case of RH exceeds 100%, the excess is expressed as water vapor supersaturation, S_v, with respect to liquid water instead of RH. Subsequently, the water vapor condenses onto surfaces provided by a subset of the preexisting aerosol particles that act as cloud condensation nuclei (CCN). The condensation of water vapor on CCN and the subsequent activation and growth of cloud droplets are described by the Köhler theory (Köhler, 1936). This theory quantifies the equilibrium S_v (or equilibrium RH) over an aqueous solution droplet as a function of droplet size, accounting for curvature (Kelvin) and solute (Raoult) effects. It defines the critical S_v at which CCN particles are activated to form cloud droplets. Due to the particle size dependence, the growth of solution droplets and S_v beyond diameters of about 1-2 µm are mostly determined by the thermodynamic state of the cloudy air parcel rather than by the physicochemical properties of the original CCN particles (Khain and Pinsky, 2018; Petters and Kreidenweis, 2007; Pinsky et al., 2012).

Despite extensive efforts during numerous field campaigns, airborne in situ measurements of S_v in clouds are highly uncertain due to inherent instrumental limitations. RH is commonly derived from measurements of air temperature and water vapor mass mixing ratio. The uncertainties of these parameters result in errors of about 5-10 % for the calculated RH (Kaufmann et al., 2018; Namdari et al., 2025), which is much larger than the actual values of S_v typically observed in cumulus clouds (~ 0.1 - 1 %) and set in CCN counters under controlled conditions (Roberts and Nenes, 2005; Rose et al., 2008). Thus, S_v at bases of warm (i.e., only liquid water containing) clouds often needs to be estimated using numerical modeling and parameterizations based on Köhler theory.

Microphysical cloud models [e.g., (Khain and Pinsky, 2018; Korolev and Mazin, 2003)] explicitly calculate the water vapor budget for adiabatic changes of thermodynamic state of a saturated air parcel where the condensational growth of cloud droplets is controlled by S_v. Based on the thermodynamic equations governing air temperature, water vapor mixing ratio and the Clausius-Clapeyron relation, the prognostic water vapor budget during cloud formation can be calculated as a function of the change in S_v per unit time:

$$\frac{dS_v}{dt} = P - C_d. \quad (1)$$

P (production term) represents the increase of S_v by cooling during the adiabatic ascent ($P = A_1 \cdot w$), and C_d (condensation term) describes the decrease of S_v due to the condensation of water vapor on CCN particles and droplets ($C_d = A_2 \cdot d(LWC)/dt$) (see Appendix A). A_1 and A_2 are thermodynamic coefficients associated with the Clausius–Clapeyron equation

describing the dependence of saturation water vapor pressure on temperature. w is the updraft velocity (dz/dt) of the rising air parcel (z represents altitude, and t time) and LWC represents the liquid water content.

For a warm cloud base, S_v is typically inferred through parameterizations that associate parcel dynamics (i.e., w) and CCN properties to droplet activation (Ghan et al., 2011; Reutter et al., 2009; Twomey, 1959). Twomey (1959) first formulated a parameterization relating the CCN spectrum to the S_v in a rising cloud parcel. The parameterization established a practical basis for predicting the number concentration of droplets (N_d) at cloud bases from CCN properties just below cloud bases and w in cloud. From this information, the S_v activation spectra of number concentration of CCN [$N_{CCN}(S_v)$] are estimated for different atmospheric conditions. Several studies based on Twomey's parameterizations have been widely implemented in cloud microphysical schemes (Ervens et al., 2010; Feingold and Heymsfield, 1992; Ghan et al., 2011; Khain et al., 2015; Reutter et al., 2009; Varghese and Prabhakaran, 2025), either in their original form or through modifications that account for additional processes such as entrainment of dry air and CCN chemical composition. These parameterizations are typically validated through so-called N_d closure analysis, where simulated and measured N_d are adjusted. The agreement achieved from this closure ranges between 20-30 %. Furthermore, $N_{CCN}(S_v)$ spectra are estimated based on satellite retrievals (Rosenfeld et al., 2016), in which clouds are considered as CCN chambers and thermodynamic as well as microphysical properties estimated for cloud bases are implemented to calculate $N_d(S_v)$ (Konwar et al., 2012; Pinsky et al., 2012; Rosenfeld et al., 2014; Zheng and Rosenfeld, 2015). The accuracy of satellite retrievals of $N_d(S_v)$ is about 25-30 % when compared with ground-based $N_{CCN}(S_v)$ measurements.

Modeling and observational studies have been performed to improve our understanding of the relationship between aerosol particle properties and their ability to form cloud droplets as a function of S_v (Ervens et al., 2010; Kleinheins et al., 2025; Kulkarni et al., 2023; Pöhlker et al., 2016; Rissler et al., 2004; Wang et al., 2008). These studies compare the predicted CCN number concentrations derived from Köhler theory, as a function of particle size and chemical composition, with results from CCN counting instruments at different S_v. N_d at cloud bases is commonly calculated in adiabatic cloud models based on the hygroscopic growth of CCN particles within a rising humid air parcel with a prescribed hygroscopicity (κ) of the CCN particles and w (Braga et al., 2021a; Pöhlker et al., 2021; Reutter et al., 2009; Varghese and Prabhakaran, 2025). These models simulate the expansion and the corresponding cooling of the air parcel, the resulting changes in RH, and the activation followed by condensational growth of cloud droplets. From closure analysis using adiabatic parcel model results, Braga et al., (2021a) observed that w and κ are critical factors in determining N_d at cloud bases, particularly in the unique environments of the Amazon Basin during the dry (polluted) season and the clean conditions of the Atlantic Ocean. The results indicated that while larger accumulation mode CCN particles dominate cloud formation over land, smaller Aitken mode CCN particles play a significantly role in cleaner marine air masses. A dedicated analysis confirming these findings is described by Pöhlker et al. (2021). The authors conclude that while w and κ are critical for CCN activation into cloud droplets, the contribution of Aitken mode particles is most significant in clean environments or deep convective clouds. Conversely, in polluted air masses, high concentrations of larger particles suppress the S_v required to activate smaller ones.

Through this sensitivity analysis, the authors clarify the thresholds where aerosol properties and w interact to determine cloud microphysics responses.

In general, current estimates of S_v at cloud base are inferred from aerosol-activation parameterizations or cloud parcel models rather than being directly constrained by independent in situ measurements (Campos Braga et al., 2017; Pinsky et al., 2012; Rosenfeld et al., 2016; Twomey, 1959; Varghese and Prabhakaran, 2025). Although these approaches reproduce observed N_d at cloud base, direct observational validation of S_v remains challenging (Campos Braga et al., 2017; Braga et al., 2021). For in situ cloud-base conditions, the quasi-steady supersaturation (S_{QSS}) is also not applicable within the activation layer because it requires dynamical forcing and the droplet population to vary slowly relative to the supersaturation-adjustment timescale, a condition that is not satisfied during rapid aerosol activation at cloud base (Romps et al., 2023; Romps, 2025).

In this study, we propose a new method to derive S_v at cloud bases for saturated parcels considering the energy and water vapor budgets during the condensational growth process of liquid droplets. S_v is diagnosed from the thermodynamic states of the saturated parcel, and the transition from the saturated-vapor state to the vapor-liquid state is treated as quasi-isobaric over the short cloud-base transition ($\Delta z \approx 10$ m), for which the expected hydrostatic pressure change is of the order 1 hPa ($\Delta p \approx \rho g \Delta z$), corresponding to ~ 0.1 % of the ambient pressure. At cloud base, in situ measurements typically show slightly lower air pressure in cloudy than cloud-free air, with higher LWC and water vapor mixing ratios at lower temperatures for quasi-isobaric conditions. The diagnostic thermodynamic state of the saturated parcel is determined primarily by the atmospheric air pressure (p), the initial air parcel temperature (T_0) of the saturated-vapor state, and the final temperature (T) of the vapor-liquid state, which constrains the calculation of the saturation ratio. At cloud base level, the atmospheric pressure and the specific heat capacity of cloudy air ($c_{p,cloud}$) vary only slightly over the short-saturated transition. Therefore, this formulation represents a quasi-isobaric thermodynamic transition rather than an extended moist-adiabatic ascent in which the temperature difference between the two thermodynamic states is directly related to vertical displacement through the saturated adiabatic lapse rate. Within this quasi-isobaric framework, the thermodynamic transition between saturated-vapor and vapor-liquid states is then constrained by the parcel energy budget.

2 Thermodynamic framework and measurement strategy

Here, the transition of thermodynamic states is assumed to be adiabatic and reversible, such that it follows an idealized reversible thermodynamic process, and the initial saturated-vapor state can be recovered from the vapor-liquid state by reversing the energy transformation. The energy associated with the vapor-to-liquid transition is constrained by the sensible enthalpy difference ($\mathrm{d}H$) between the two thermodynamic states and by the latent energy released during condensation (Q), such that $\delta Q = \mathrm{d}H$. Q is interpreted as an internal energy redistribution within the parcel rather than as external diabatic heating. The partitioning of the condensational energy of the saturated parcel is formulated from the first law of

thermodynamics, such that the latent energy associated with condensation, Q, is partitioned between changes in parcel internal energy (ΔU) and the work associated with water vapor expansion (W_s), according to $Q = \Delta U + W_s$. Within this diagnostic framework, part of the condensational energy is associated with W_s during liquid-water formation relative to the limiting case in which the entire condensational energy contributes to liquid formation ($\delta Q = dH$). Consequently, the LWC is reduced, resulting in a relative excess of water vapor. We define the cloud supersaturation (S_c) from the vapor pressures of the saturated parcel in the vapor and liquid states for the limiting case in which the entire condensational energy contributes to liquid formation. Since part of Q is associated with W_s during the vapor-to-liquid transition, we diagnostically define the liquid-phase supersaturation (S_l) and vapor-phase (S_v) as the respective fractions of Q associated with ΔU and W_s (i.e., $S_c = S_l + S_v$). The corresponding temperatures of the vapor and liquid states obtained from the energy-budget calculations define the vapor pressures of the saturated parcel during the vapor-to-liquid transition.

The derived S_v provides a thermodynamic analogue to the effective supersaturation established in a CCN counter (CCNc), where the instrument supersaturation is calibrated from the critical activation of particles with known physicochemical properties, e.g. ammonium sulfate, using Köhler theory (Roberts and Nenes, 2005; Rose et al., 2008). This correspondence allows the cloud-base N_d (S_v) relationship to be represented by the classical power-law CCN activation spectrum, $N_d = C \cdot S^k$ (Twomey, 1959), in which increasing supersaturation activates progressively larger fractions of the available CCN population. Unlike conventional parcel-model or CCN-closure approaches, which estimate S_v from prescribed w and CCN properties to reproduce the observed N_d, the present method diagnoses cloud-base S_v from a thermodynamic energy-budget closure constrained primarily by condensational energy and LWC. The method is evaluated using in situ measurements of cloud-base properties and compared with N_{CCN} (S_v) observations below cloud base. In this framework, Q is directly derived from measured LWC, air temperature (T) and pressure (p) at cloud base, while T_0, ΔU, W_s, S_l, and S_v are diagnostically estimated. The airborne cloud base data were collected in growing convective cumuli over the Amazon Basin in September 2014 during the ACRIDICON-CHUVA campaign (Wendisch et al., 2016), encompassing polluted conditions over forested and deforested regions, and clean marine conditions over the adjacent Atlantic Ocean. ACRIDICON stands for "Aerosol, Cloud, Precipitation, and Radiation Interactions and Dynamics of Convective Cloud Systems"; CHUVA is the acronym for "Cloud Processes of the Main Precipitation Systems in Brazil: A Contribution to Cloud Resolving Modeling and to the GPM (Global Precipitation Measurement)". The High Altitude and Long Range Research Aircraft (HALO) was used during the campaign (Stevens et al., 2019). The resulting cloud-base N_d (S_v) spectra was calculated for eight flight segments and, for the flights in the Central Amazon, were compared with the N_{CCN} (S_v) spectra measured below cloud base. This comparison tests the robustness of the underlying physical assumptions, as the cloud-base N_d (S_v) spectrum is expected to represent the N_{CCN} (S_v) population below cloud bases. Figure 1 summarizes the measurement strategy and the diagnostic thermodynamic framework used in this study. Cloud-base measurements provide N_d, LWC, T, and p while N_{CCN} (S_v) is independently measured below cloud base (Fig. 1a). From the measured cloud-base state, the initial saturated-vapor state is diagnostically reconstructed under the assumptions of an adiabatic and reversible transition treated locally as quasi-isobaric (Fig. 1b). The

condensational energy is partitioned according to $Q = \Delta U + W_s$, from which the liquid- and vapor-phase contributions to cloud supersaturation, S_l and S_v, are derived. The resulting cloud-base $N_d(S_v)$ spectrum is then compared with the independently measured sub-cloud N_{CCN} (S_v) spectrum as a closure test of the proposed framework. The following section 3 presents the proposed method and its underlying physical laws, while the results and discussion are provided in the subsequent sections. Table A1 in the Appendix lists and defines the symbols used in this manuscript.

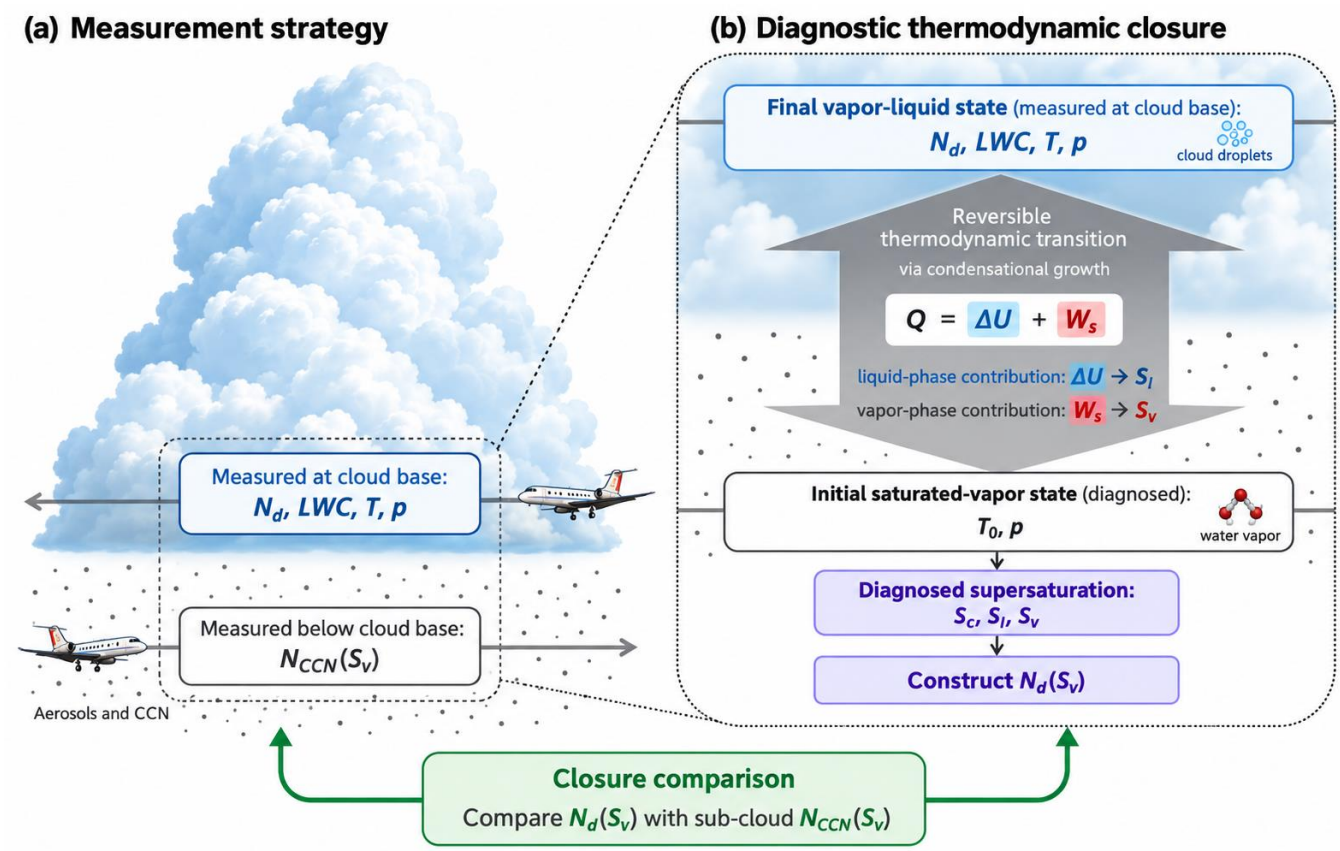

Figure 1. Measurement strategy and diagnostic thermodynamic closure used to derive water vapor supersaturation at cloud base. (a) Schematic of the airborne measurement strategy. At cloud base, the HALO aircraft measures droplet number concentration (N_d), liquid water content (LWC), temperature (T), and pressure (p). Below cloud base, cloud condensation nuclei activation spectra, N_{CCN} (S_v), and pressure are measured. The highlighted cloud-base region indicates the local layer to which the thermodynamic closure is applied. (b) Schematic of the diagnostic thermodynamic framework. The measured cloud-base state is treated as the final vapor-liquid state, characterized by N_d, LWC, T, and p, while the corresponding initial saturated-vapor state, characterized by T_0 and p, is diagnosed. The transition between these states is represented as a reversible thermodynamic transformation during condensational growth. The latent heat (Q) released by condensation is partitioned according to $Q = \Delta U + W_s$, where the internal-energy contribution is associated with the liquid-phase supersaturation S_l and the water-vapor expansion work with the vapor-phase

supersaturation S_v. The diagnosed supersaturations S_c, S_l, and S_v are then used to construct the cloud-base N_d (S_v) spectrum, which is compared with the independently measured sub-cloud N_{CCN} (S_v) spectrum as the closure test.

3 Methods

We present a physically based diagnostic formulation to derive S_v at cloud bases in a saturated air parcel (with respect to water vapor over a plane liquid water surface). The formulation couples the parcel energy and water vapor budgets during the condensational growth. Across the analyzed cloud base transition, pressure variations are typically small of the order of 0.1 % of the atmospheric pressure; the process is therefore treated locally as quasi-isobaric. The transition is further assumed to be adiabatic and reversible, and the total moist enthalpy approximately conserved over the short cloud-base transition, while the sensible enthalpy changes between the saturated-vapor and vapor-liquid states. In the energy budget, the condensation energy (Q) is treated as a partition between the change in internal energy (ΔU) associated with the transition between the thermodynamic states, and the work associated with water vapor expansion (W_s). Under saturated quasi-isobaric conditions, the energy budget is governed by pressure and temperature, and the partitioning between ΔU and W_s remains process-dependent. The energy budget is diagnosed from the temperature change between the thermodynamic states, which determines the sensible enthalpy difference (dH), and equivalently, from the condensational energy (Q) for a given liquid water content. The cloud supersaturations (S_c, S_l and S_v) are then diagnostically calculated from the resulting energy and water vapor budgets during the condensational growth process. In this study, the variables are expressed as specific quantities per unit mass of dry air and are denoted by uppercase symbols. To recover the corresponding extensive quantities, these terms must be multiplied by the mass of dry air.

In situ measurements at the cloud bases of growing cumulus clouds are used to evaluate the theoretical assumptions. N_{CCN} (S_v) spectra measured just below cloud base, prior to cloud measurements, are compared with the N_d (S_v) spectra derived at cloud base during flights in the Central Amazon. The N_d (S_v) spectrum is considered representative of the N_{CCN} (S_v) population below cloud base that, after buoyant ascent, is activated into cloud droplets. The analysis is restricted to the cloud-base activation stage, where sub-cloud CCN can be related most directly to newly formed droplets. Farther above cloud base, the effects of entrainment of dry air, evaporation, secondary activation of CCN and coagulation processes weaken this correspondence. The following subsections describe the steps of the proposed method, its underlying physical formulation, and the cloud, meteorological, and CCN measurements used in this study.

3.1 *Calculation of the latent heat of condensation*

The total energy of the saturated parcel is limited by the sensible enthalpy difference of the phase change from vapor to liquid, $\delta Q = dH$, and can be written in finite forms as follows (hereafter the signs in the energy balance equations describe the direction of energy transfer):

$$\delta Q = dH \quad \therefore \quad L_v \cdot q_l = -\, c_{\mathrm{p,cloud}} \cdot \Delta T = -\, c_{\mathrm{p,cloud}} \cdot (T_0 - T). \qquad (2)$$

Where q_l is the liquid water mixing ratio (kg kg^{-1}), $c_{\mathrm{p,cloud}}$ is the specific heat capacity of cloudy air (J kg^{-1} K^{-1}), and L_v is the latent heating of vaporization (J kg^{-1}). The q_l and $c_{\mathrm{p,cloud}}$ are defined as the following:

$$q_l = LWC/\rho_{\mathrm{air}}, \quad (3)$$

and,

$$c_{p,cloud} = c_{pd} + c_{pv} \cdot r_s + c_{pl} \cdot q_l. \quad (4)$$

Where, ρ_{air} is the dry air density (kg m^{-3}), LWC is the liquid water content (kg m^{-3}), r_s is the saturation water vapor mixing ratio (kg kg^{-1}), c_{pd} is the specific heat of dry air at constant pressure (1005 J kg^{-1} K^{-1}), c_{pv} is the specific heat of water vapor at constant pressure (1850 J kg^{-1} K^{-1}), c_{pl} is the specific heat of liquid water at constant pressure (4218 J kg^{-1} K^{-1}). We assume the warmer temperature (T_0) in the $c_{\mathrm{p.cloud}}$ and L_v calculations, as it represents the initial condition of the saturated parcel. For small temperature differences at cloud base (< ~1 K), $c_{\mathrm{p.cloud}}$ varies only weakly with r_s and q_l. Since T and T_0 represent the temperatures of a saturated parcel under isobaric conditions, they are equivalent to the dew-point temperature at the corresponding pressure. Furthermore, r_s is calculated as follows:

$$r_s = (R_d/R_v) \cdot \frac{e_s(T)}{p - e_s(T)} \qquad (5)$$

Where R_v is the gas constant for water vapor (461.5 J kg^{-1} K^{-1}), R_d is the gas constant for dry air (287.05 J kg^{-1} K^{-1}), and $e_s(T)$ is the saturation water vapor pressure (Pa) (Bolton, 1980; Rogers and YAU, 1989). The values of e_s can be calculated for a wide range of temperatures in Celsius (-30 °C ≤ T_c ≤ 35 °C) with minor uncertainties (~ 0.1 %) as follows:

$$e_s = 611.2 \cdot exp\left(\frac{17.67 \cdot T_c}{T_c + 243.5}\right) \qquad (6)$$

During the phase change, the internal energy decreases ($T_0 > T$) as q_l and Q increase. The phase change process leads to an increase in the air temperature, represented here by the latent-heat-equivalent temperature (T_Q), which is approximately conserved during the vapor-to-liquid conversion, i.e.:

$$T_Q = T + \Delta T_Q \approx T_0 \quad (7)$$

Where, $\Delta T_Q = \frac{L_v \cdot q_l}{c_{p,cloud}}$ (8)

3.2 *Cloud supersaturation*

The formulation of RH describes the amount of water vapor in the air relative to the maximum amount of water vapor the air can hold for a given temperature, i.e., the saturation ratio, and is defined as follows:

$$RH = 100 \cdot \frac{e(T)}{e_s(T)} \quad [\%] \quad (9)$$

Where $e(T)$ is the ambient water vapor pressure (Pa). For a saturated parcel or cloud undergoing cooling (from T_0 to T) the reference-state saturation ratio (RH_c) is calculated as follows:

$$RH_c = 100 \cdot \frac{e_s(T)}{e_s(T_0)} \quad [\%] \quad (10)$$

and the cloud supersaturation (S_c) is formulated as follows:

$$S_c = RH_s - RH_c = 100 - RH_c \quad [\%] \quad (11)$$

where RH_s = 100 % is the saturation ratio at the reference state (T_0), and S_c expresses the thermodynamic excess of water vapor relative to equilibrium with respect to liquid water at the reference state. Since the cooling process is related to the increase of q_l (shown in Eq. 2), the increase in S_c is associated with vapor-to-liquid conversion and Q.

3.3 *Calculation of energy budget from the first law of thermodynamics*

According to the first law of thermodynamics, the change in internal energy of a closed system is determined by the balance between heat exchange and pressure-volume work. For an isobaric process involving only pressure-volume work, the change in sensible enthalpy (dH) can be interpreted as the sum of the change in internal energy and the expansion work performed by the system. Under adiabatic conditions, the dH equals the heat exchanged at constant pressure by a saturated parcel. Thus, for a saturated parcel undergoing condensational growth from the reference state, the latent heat released (δQ = dH) is the source of heat in the thermodynamic system, and the energy budget can be calculated following the first law as follows:

$$Q = \Delta U + W_s \quad (12)$$

where Q represents the latent heat released by condensation, ΔU is the change in internal energy of the parcel associated with vapor-liquid conversion, and W_s is the specific work done by water vapor during expansion. The terms of ΔU and W_s are calculated for a saturated parcel under isobaric cooling as follows:

$$\Delta U = -\, c_{p,cloud} \cdot (T_0 - T_{ws}) \quad (13)$$

and,

$$W_s = r_s \cdot \int_{\alpha_{vs0}}^{\alpha_{vs}} e_s d\alpha_v = r_s \cdot \int_{\alpha_{vs0}}^{\alpha_{vs}} \frac{R_v \cdot T}{\alpha_v} d\alpha_v \approx r_{s0} \cdot R_v \cdot T_0 \cdot ln\left(\frac{\alpha_{vs}}{\alpha_{vs0}}\right) = r_{s0} \cdot R_v \cdot T_0 \cdot ln\left(\frac{T}{T_0} \cdot \frac{e_s(T_0)}{e_s(T)}\right) \quad (14)$$

Where α_v is the specific volume of water vapor for saturated conditions ($m^3 kg^{-1}$). The W_s term represents the effective thermodynamic work associated with changes in the specific volume of saturated water vapor during cloud-adiabatic cooling. Under quasi-isobaric conditions and small cloud base cooling intervals, the integration is referenced to the initial thermodynamic state of the saturated parcel (T_0), and W_s depends primarily on T_0 and T.

Analogous to Equation 2, the energy budget from Equation 12 can be calculated as follows:

$$L_v \cdot q_l = - c_{p,cloud} \cdot \Delta T_{ws} + r_{s0} \cdot R_v \cdot T_0 \cdot ln\left(\frac{\alpha_{vs}}{\alpha_{vs0}}\right) \quad (15)$$

or,

$$L_v \cdot q_l - r_{s0} \cdot R_v \cdot T_0 \cdot ln\left(\frac{\alpha_{vs}}{\alpha_{vs0}}\right) = - c_{p,cloud} \cdot (T_0 - T_{ws}) \quad (16)$$

From this budget, T_{ws}, the saturated temperature, is slightly warmer than T calculated in Equation 2 due to the W_s term. Similarly, the resulting air temperature (T_{air}) will be slightly cooler than T_Q due to the W_s term. Thus, T_{air} is calculated as follows:

$$T_{air} = T_Q - \left(\frac{W_s}{c_{p,cloud}}\right) \quad (17)$$

The differences of the saturated temperatures ($T_{ws} - T$) and air temperature (T_0 -T_{air}) are the same.

3.4 *Reversibility of the saturated parcel energy budget*

The reversibility of the energy budget for isobaric conditions relies on the fact that the magnitude of the total latent energy ($\delta Q = dH$) can be expressed equivalently in terms of either LWC or the temperature difference (ΔT) between two saturated states. In Section 3.1, we show that the relationship between LWC and ΔT is one-to-one since the parameters are calculated as a function of the initial thermodynamic properties of the saturated parcel. In this framework, this dependence is treated explicitly through an iterative solution, ensuring consistency between condensate and heat capacity.

When the total energy is partitioned as $Q = \Delta U + W_s$, the internal-energy component represents a reduced cooling of the saturated parcel compared to the case without accounting for the work term W_s. Despite this partitioning, the functional dependence between q_l and ΔT_{ws} remains unchanged, so the relationship between thermodynamic variables remains one-to-one. Since the parameters at W_s, $c_{p,cloud}$ and L_v are calculated for the initial conditions of the parcel (T_0), the reversibility of the heat budget is preserved, ensuring a consistent and reversible relationship between condensate and temperature within

the proposed framework. The numerical differences while applying equations 2 and 12 to calculate Q are negligible (< ~ 0.01 %). The differences between the thermodynamic and energetic components of the cloud parcel for simulations with a range of initial temperatures T_0 (2°C to 30°C) and adiabatic cooling magnitudes (ΔT) are presented in Section S1 of the Supplementary Material. The calculations are performed for the energy and vapor budgets at an atmospheric pressure of 950 hPa, similar as shown in the section 4.1.

3.5 *Calculation of liquid and water vapor supersaturation*

The calculation of liquid supersaturation (S_l) and water vapor supersaturation (S_v) from the cloud supersaturation (S_c) is performed as a function of the energy budget formulation described in section 3.3, where S_l and S_v are the energy contributions of ΔU and W_s in the total energy of the saturated parcel (Q), respectively.

The signs in the energy balance equations shown above describe the direction of energy transfer. However, S_l and S_v are not directional variables. They represent the partition of S_c considering the energy budget, which is defined from the absolute magnitudes of the energetic contributions, and thus, for a given latent heat released, due to condensation S_l and S_v are calculated as follows:

$$S_l = S_c \cdot \frac{|\Delta U|}{Q} \quad [\%] \quad (18),$$

$$S_v = S_c \cdot \frac{W_s}{Q} \quad [\%] \quad (19),$$

Where,

$$S_c = S_l + S_v \quad [\%] \quad (20)$$

3.6 *Closure analysis from airborne measurements at cloud bases*

The calculations of RH_c and cloud supersaturations (S_c, S_l, and S_v) at cloud bases are performed from measurements collected during the ACRIDICON-CHUVA campaign using HALO. Cloud probes and meteorological sensors on board HALO have been used to collect the necessary data. Table 1 summarizes the general thermodynamic conditions and time intervals of cloud properties measured at cloud bases. The cloud measurements were conducted with the Cloud Combination Probe - Cloud Droplet Probe (CCP-CDP) (Lance, 2012). In this study, we focus on the initial stage of cloud formation. Therefore, only 1 Hz cloud passes (individual in-cloud sampling intervals) with N_d greater than 20 cm^{-3}, developing under updraft conditions, are considered. This threshold of N_d = 20 cm^{-3} is used to avoid haze and well-mixed cloud elements in the analysis. Furthermore, cloud passes with measured raindrops are removed from our analysis. In the supplementary material (Section S2), we present the sensitivity analysis assuming the proposed threshold for cloud identification and varying the values of N_d and LWC for the derived supersaturations and their relationships. These analysis shows that the derived

supersaturations and their relationships assuming the proposed threshold (N_d > 20 cm^{-3}) are robust with respect to variations in cloud identification criteria. The remaining variability is primarily driven by environmental heterogeneity and turbulence rather than by the threshold definition itself.

The closure analysis relies on the reversibility of the cloud adiabatic parcel as described in section 3.4. The calculations of RH_c, S_c, S_l, and S_v require the information of p, LWC, T, and T_0 near cloud bases. From the airborne data at cloud bases, p, T and LWC are measured. The distinction between the measured cloud-base quantities and the diagnostically reconstructed thermodynamic state is illustrated in Fig.1b. Therefore, we estimate T_0 and T_{air} for each cloud pass. Below are the sequential steps used in our analysis:

1. T_0 (or T_Q) is iteratively estimated for each cloud pass from Q (calculated from LWC, T and p) using Eq. 2. RH_c and S_c are subsequently calculated from T and estimated T_0.
2. The process is repeated by considering both Q, calculated in the first step, and W_s in the energy budget (see Eq. 16), which results in an estimated air temperature (T_{air}) lower than T_0 obtained in step 1, such that $T_0 > T_{air} > T$. From this closure analysis, the values of ΔU and W_s are estimated, and S_l and S_v are subsequently calculated with Eqs. 18 and 19, respectively.

During flights AC11, AC14 and AC17, the $N_{CCN}(S_v)$ spectra from two CCN counters (CCNa and CCNb) were measured below cloud base prior to cloud base measurements with the CCP-CDP probe. This comparison provides an important evaluation of the derived water vapor component of cloud supersaturation (S_v), since CCN chamber measurements are independent of in-cloud condensational growth processes. The $N_d(S_v)$ spectra were converted to standard temperature and pressure (STP) conditions before comparison. The comparison between $N_d(S_v)$ and $N_{CCN}(S_v)$ aimed to evaluate the physical consistency of the proposed thermodynamical framework. In the CCN counters, S_v is determined from the Köhler theory using particles with a known physicochemical composition, typically ammonium sulfate, and is therefore independent of cloud processes.

3.7 *Aircraft data*

3.7.1 Meteorological measurements

HALO was equipped with a meteorological sensor system (BAsic HALO Measurement And Sensor System– BAHAMAS) located at the nose of the aircraft (Wendisch et al., 2016). The water vapor mixing ratio and derived humidity quantities were measured by the Sophisticated Hygrometer for Atmospheric Research (SHARC). The uncertainties for measurements at a frequency resolution of 1 Hz of air pressure, air temperature, relative humidity, water vapor mixing ratio, and wind speed are about 3 Pa, 0.5 K, 5 %, 4% and 0.3 m s^{-1}, respectively (Mallaun et al., 2015).

3.7.2 Cloud and CCN measurements

The measurements of cloud properties over the Amazon Basin were performed at a frequency resolution of 1 Hz by the CCP mounted below the wings of the aircraft (Lance, 2012). CCP combines two detectors, the CDP and the grayscale Cloud Imaging Probe (CIPgs), which allow the measurement of droplets with a size range of 3-960 µm. In this study, the integrated water content of CDP for bin diameters ranging from 3-50 µm was used to calculate the *LWC* at warm cloud bases. The measurements were validated by another cloud probe (Cloud and Aerosol Spectrometer with depolarization, CAS-DPOL) and a hot wire King probe (Campos Braga et al., 2017). The integrated water content of CIPgs for bin diameters greater than 50 µm was used to calculate the Rainwater Content (*RWC*). Only cloud passes without rain droplets (i.e., $RWC = 0$ g m^{-3}) are used in our analysis.

During the ACRIDICON-CHUVA campaign, CCN number concentrations were measured at a frequency resolution of 1 Hz onboard HALO using a two-column CCNc [CCN-200; columns A (CCNa) and B (CCNb)], which is a continuous-flow longitudinal thermal-gradient instrument manufactured by Droplet Measurement Technologies (DMT) (Roberts and Nenes, 2005). In the instrument, the sampled aerosol particles are exposed to a set supersaturation and absorb water depending on their size and chemical composition. Particles that grow to droplets larger than 1 µm in diameter are counted as CCN at that S_v. CCNa measured CCN concentrations with cycled S_v between 0.2 and 0.55 % at 100 s intervals, and CCNb measured CCN concentrations with a fixed $S_v \sim 0.55$ %. Table 2 summarizes the general thermodynamic conditions and the time intervals during which CCN measurements were conducted below cloud base. The N_{CCN} (S_v) measurements of the chambers were compared to the measured N_d and calculated S_v for three flights where $N_d(S_v)$ and N_{CCN} (S_v) had the same range of S_v values.

For measurements on polluted conditions during flights AC11, AC14 and AC17, the estimated uncertainties in CCN concentrations are about 10 %. Furthermore, the estimated relative uncertainty in S_v values (σ_{sv}/S_v) is about 14 % on average, resulting from the uncertainties of 10 % from counting efficiencies and 10 % due to calibration accuracy. Sample air for the aerosol measurements was obtained from two different inlets: (i) the HALO aerosol submicron inlet (HASI) and (ii) the HALO counterflow virtual impactor (HALO-CVI). The CCN-200 provides the possibility to measure from both inlets in parallel or at two different values of S_v.

3.7.3 Airborne meteorological and cloud properties uncertainties

During the ACRIDICON–CHUVA campaign, the resulting uncertainty in the measured N_d and *LWC* by CCP–CDP with 1 Hz resolution was about 10 % (Campos Braga et al., 2017). The uncertainty of *RWC* measurements was about 30 % (Braga et al., 2017b, 2021b). *RWC* uncertainties are less relevant to this study since we are focused on shallow cumulus clouds in the initiation stage of development, which typically have no rain droplets.

The measurement uncertainties of the energy budget parameters were calculated using a Monte Carlo method (JCGM, 2008) and are described in section S2.2 in the Supplementary Material. The uncertainties in the meteorological measurements from the BAHAMAS system translate into an estimated average uncertainty of about 0.24 percentage points (%) (typically < 1 % for 1 Hz data) in the derived RH_c. The relative uncertainties in the energy terms are about 10 % for Q and ΔU, and 13 % for W_s. Propagating these errors yields relative uncertainties of supersaturation (σ_s/S) of approximately 10 % for S_c and S_l, and ~12 % for S_v. The uncertainties of energy terms and supersaturations are primarily sensitive to the LWC uncertainties. Baumgardner et al. (2017) reports that expected range of uncertainties in LWC and N_d is between 10 % and 30 %. For LWC uncertainty of 30 %, the relative uncertainties of the energy terms are about 29 % for Q and ΔU, and 38 % for W_s. Propagating these errors yields overall uncertainties of ~28 % for S_c and S_l, and ~36 % for S_v.

The uncertainties of the power-law relationship $N_d = C \cdot S_v^{\,k}$ fitted for each flight segment shown in this manuscript were also calculated using Monte Carlo uncertainty propagation (using 10 % for N_d and 12.6 % for S_v). These calculations are presented in Section S2.3 of the Supplementary Material. Across all flights, the exponent is well constrained with uncertainties of $\sigma k \approx 0.01$–0.03, while the C shows relative uncertainties of approximately 2–6 %. Higher measurement uncertainties increase the scatter in the power-law relationships N_d - S (shown in Tables S5-S7). Our analysis show a systematic decrease in both C and k when uncertainties increase, indicating that uncertainty propagation affects not only the precision but also the magnitude of the fitted parameters. Despite these shifts, the power-law relationship remains consistent across thresholds and flights, and the variations in C and k are within the broader uncertainty range of the estimates. This indicates that while increased uncertainties reduce the strength of the statistical fit and slightly bias the parameter values, they do not alter the underlying physical dependence of N_d on S_c, S_l, and S_v.

Table 1. Summary of cloud base 1 Hz CCP-CDP measurements conditions, including sampling duration and mean thermodynamic conditions for each analysed flight segment.

Flight	Date in 2014	Initial Time (UTC)	End Time (UTC)	Duration of Measurements (s)	Average Altitude (m)	Average Pressure (hPa)	Average Temperature (°C)
AC07	6-Sep	17:58:00	18:12:50	77	1910	812.3	16.2
AC09	11-Sep	15:41:10	15:53:20	41	1220	878.85	19.5
AC11	16-Sep	17:53:00	18:05:50	33	1896	812.28	16.2
AC14	21-Sep	15:36:40	15:57:30	73	1602	843.4	17.67
AC17a	27-Sep	15:11:40	15:28:40	121	1589	843.28	17.6
AC17b	27-Sep	17:07:00	17:17:00	64	1902	812.3	16.15
AC18	28-Sep	16:46:05	16:55:40	99	1711	834.07	17.18
AC19	30-Sep	17:27:50	17:37:40	163	606.5	942.59	22.26

Table 2. Summary of below cloud base 1 Hz CCN measurement conditions, including sampling duration and mean thermodynamic conditions for each analysed flight segment.

Flight	Date in 2014	Initial Time (UTC)	End Time (UTC)	Duration of Measurements (s)	Average Altitude (m)	Average Pressure (hPa)	Average Temperature (°C)
AC11	16-Sep	17:39:10	17:50:00	650	450.93	958.91	28.06
AC14	21-Sep	15:25:00	15:33:20	500	954.9	908.77	22.85
AC17a	27-Sep	14:55:00	15:06:40	700	941.81	908.77	22.87
AC17b	27-Sep	16:52:30	17:01:40	550	1255.4	875.67	21.85

4 Results

4.1 *Energetic budget and supersaturations at cloud base*

To illustrate the thermodynamic basis of the energetic budget analysis at cloud base, we first describe the fundamental relationships between the initial temperature of the saturated parcel (T_0) and adiabatic cooling ΔT for T_0 ranging from 2°C to 30°C. Figure 2 shows the simulated values of LWC, Q, ΔU, and W_s resulting from the energy balance at a pressure level of 950 hPa. All quantities from the energy balance are expressed as positive values to represent the partition of the total energy (Q) during the condensational growth. In the case in which water vapor is completely condensed ($Q = \mathrm{d}H$) the LWC (solid lines) increase almost linearly with cooling rate for different T_0. For the same cooling rate, a slightly larger LWC is calculated for lower temperatures owing to the higher dry air density of the saturated parcel. When accounting for W_s in the energy budget, the resulting values of LWC (dotted lines) are relatively smaller. At 950 hPa, the fractional reduction in LWC due to W_s increases approximately linearly with temperature, ranging from about 4-6% at low temperatures (~ 2-6 °C) to 15-20% at higher temperatures (~ 25-30 °C) (see Figure S1). The values of ΔU are slightly smaller than Q since the total energy is partitioned with W_s, which increases approximately linearly with temperature and logarithmically with the cooling rate.

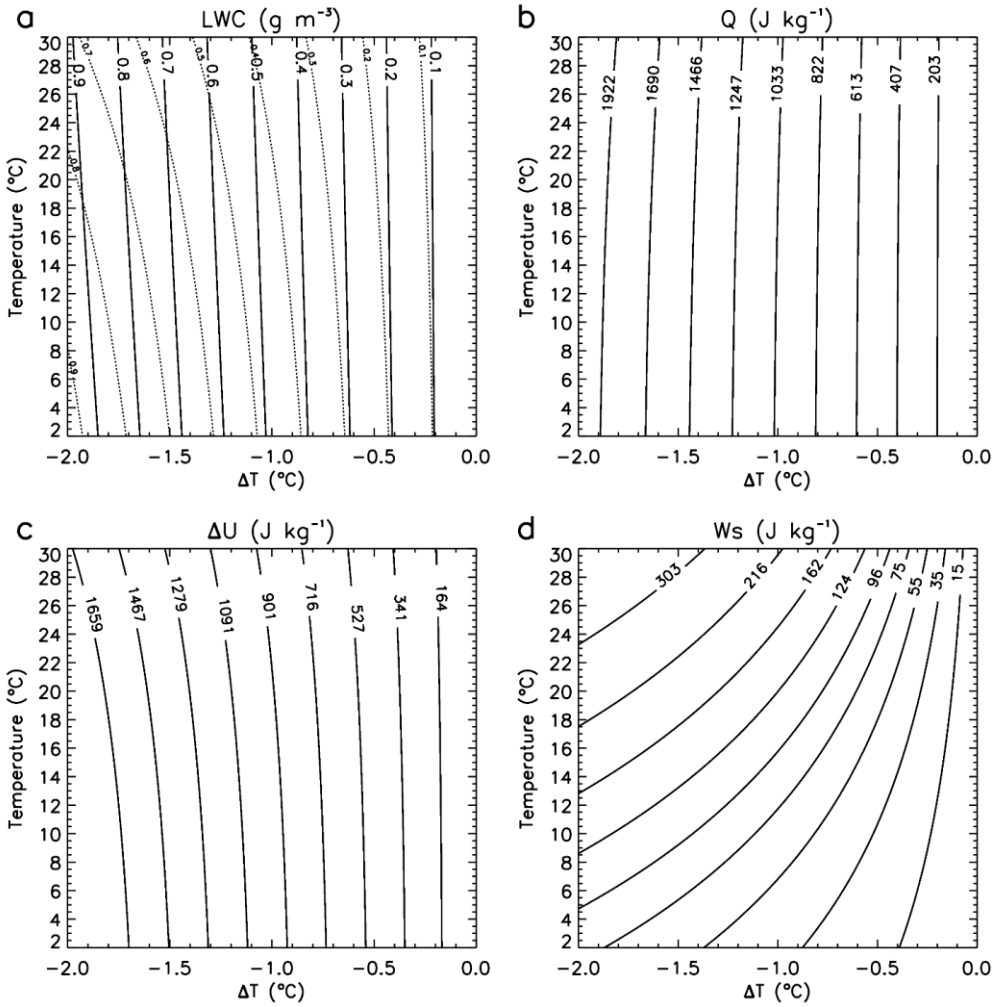

Figure 2. (a) Contours of Liquid Water Content (*LWC*) values of cloud adiabatic parcels as a function of initial temperature T_0 (y-axis) and adiabatic cooling rate (ΔT) (x-axis) at 950 hPa. Dotted lines indicate the *LWC* resulting from the energy budget (W_s term leads to *LWC* decrease for the same ΔT). Similar for (b) Latent heat of condensation (*Q*), (c) Magnitude of internal-energy change ($|\Delta U|$), and (d) saturation work (W_s).

Figure 3 shows the corresponding values of RH_c, S_c, S_l, and S_v derived from the energy budget framework. Figures 3a-b show RH_c decreasing below 100%, with a corresponding increase of S_c above 0% as a function of the prescribed adiabatic cooling. For a given cooling magnitude, the increase in S_c becomes slightly smaller at warmer temperatures because the fractional reduction in RH_c $[e_s(T)/e_s(T_0)]$ for a fixed ΔT decreases slightly with increasing T_0, consistent with the temperature dependence of the Clausius-Clapeyron relation. Figures 3c-d show the partitioning of S_c into S_l and S_v resulting

from the energy budget analysis. The values of S_l are about one order of magnitude larger than S_v, indicating that most of the enthalpy change associated with adiabatic cooling and condensation contributes to vapor-to-liquid conversion and condensational growth, while W_s represents a smaller fraction of the total energy budget. Since W_s increases with T_0, S_v becomes relatively larger under warmer cloud-base conditions for the same cooling magnitude, whereas the opposite behaviour is observed for S_l. This emphasizes the increasing contribution of saturation work to the total energy budget at warmer temperatures, which enhances S_v while reducing the condensational growth of cloud particles.

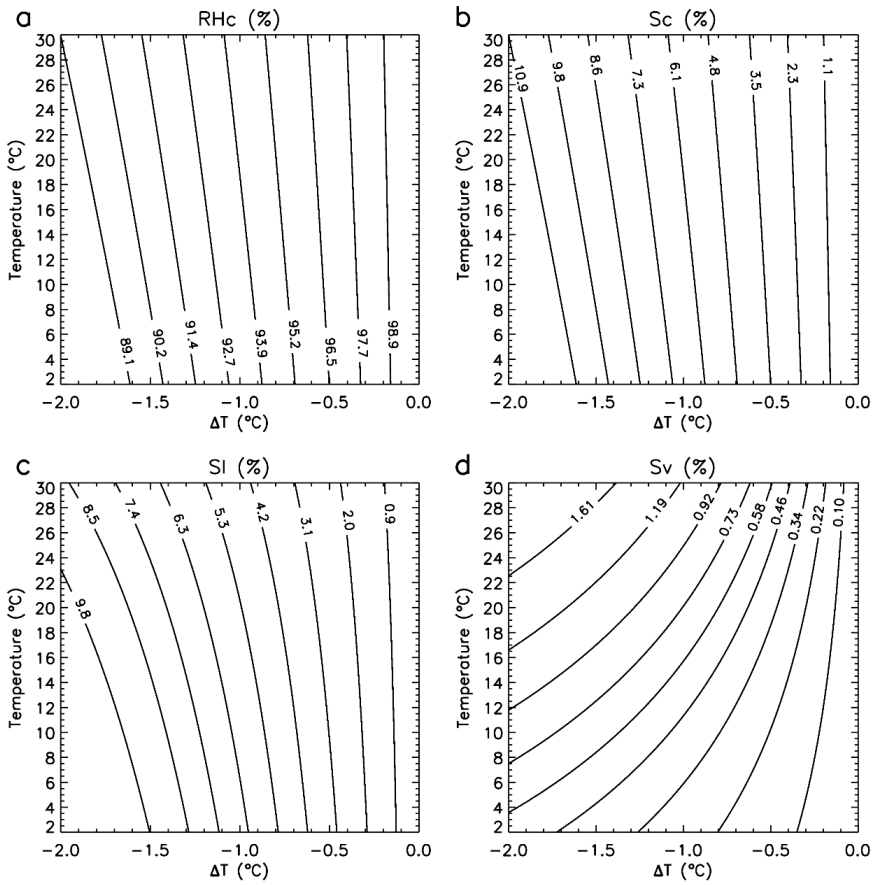

Figure 3. (a) Contours of reference-state saturation ratio (RH_c) as a function of initial temperature T_0 (y-axis) and adiabatic cooling rate (ΔT) (x-axis) for saturated parcels at 950 hPa. (b), (c) and (d) Similar to cloud supersaturation (S_c), liquid-phase supersaturation (S_l), and for water vapor supersaturation (S_v), respectively.

These relationships between energetic partitioning and the vapor budget remain qualitatively similar under lower-pressure conditions. However, as pressure decreases, the *LWC* is reduced because the density of dry air decreases. Furthermore, for a given T_0 and ΔT, the magnitude of W_s is slightly enhanced at lower pressures due to the larger saturation mixing ratio (see

Eq. 5), thereby increasing the contribution of water vapor expansion to the total energy budget. Consequently, a smaller fraction of the enthalpy change associated with cooling and condensation contributes to vapor-to-liquid conversion and condensational growth. At 850 hPa, for example, the reduction in *LWC* associated with W_s ranges from approximately 5-7 % at low temperatures (~ 2-6 °C) to about 18-22 % at higher temperatures (~ 25-30 °C) (Figure S2). The larger contribution of W_s to the energy budget leads to slightly larger S_v and smaller S_l relatively to those at 950 hPa.

4.2 *Cloud supersaturations at cloud bases of growing cumuli*

The data collected during the ACRIDICON-CHUVA campaign over the Amazon Basin provides a particularly useful testbed for the cloud base closure analysis because the same aircraft and instrumentation sampled a wide range of cloud base environments, from relatively clean marine and forested conditions to polluted air masses influenced by biomass burning and the Manaus urban plume (see the locations of the cloud base measurements at Fig. S3).

Figure 4 illustrates a case study of the dependence of N_d at cloud base on RH, RH_c, cloud supersaturations (S_c, S_l, S_v), and the associated energetic terms (Q, ΔU, W_s) derived from measurements collected during Flight AC14. During this flight leg, cloud bases of developing cumuli were sampled under RH conditions ranging from ~ 60 % to ~ 102 %, at an altitude of about 1600 m and temperatures near 17.6 °C. Figure 4a shows that RH generally increases as a function of N_d even though in most cloud passes RH is smaller than 100 %. This variability in RH measurements arises from the characteristics of in situ temperature measurements: liquid water impinging on the sensor can induce evaporative cooling, whereas the latent heat released during particle condensational growth and buoyant air volumes may locally warm the sensor. RH_c decreases consistently with N_d associated with higher *LWC*. For cloud passes where $RH < RH_c$ the local vapor pressure $e(T)$ is typically smaller than expected from the cooling trajectory of the initially saturated parcel, suggesting enhanced entrainment of unsaturated environmental air and reduced condensational growth (see Figure S4). Under such conditions, smaller droplets evaporate preferentially due to the inhomogeneous nature of mixing in convective clouds. This selective evaporation reduces the local *LWC*, and the remaining droplet population is biased toward droplets formed on CCN with higher hygroscopicity, which are more resistant to evaporation. Conversely, cases in which $RH > RH_c$ indicate that the parcel retains a larger vapor content relative to theoretical calculations, favouring continued condensational growth, enhanced S_v, yielding higher N_d for a given CCN population.

Figure 4b shows the dependence of N_d on S_v and S_l at cloud base. Both S_l and S_v increase with N_d, although S_v remains nearly one order of magnitude smaller than S_l. The calculated S_v values exhibit the expected positive relationship between supersaturation and droplet concentration commonly observed in CCN activation spectra. The $N_d(S_v)$ relationship exhibits substantial variability at cloud base owing to the inhomogeneous and turbulent nature of the in situ measurements. The dispersion is particularly enhanced for cases in which relatively large N_d values are associated with small S_v, corresponding to conditions where the local vapor pressure remains below the theoretical simulations ($RH < RH_c$). Nevertheless, most of the measured water vapor pressures remain within the estimated uncertainty range of the theoretical estimates (see Fig. S4),

indicating that the overall N_d-S_v relationship remains representative of the cloud base thermodynamic conditions. Figure 4c presents the energy budget components as a function of S_c, while Figure 4d depicts the cloud supersaturations derived from the measured *LWC*. These figures show that the total energy (Q) increases strongly with *LWC* and is dominated by changes in internal energy ($\Delta U/Q$; ~ 90 % on average), while the contribution from saturation work (W_s) is comparatively minor.

Similar characteristics of the energy budget were observed for the different flight legs measured in the Amazon Basin and Atlantic Ocean (Figures S5-S18). In these flight segments, most of the measured water vapor pressures were within the estimated uncertainty range of the theoretical cloud-adiabatic estimates. The estimated fraction of $\Delta U/Q$ accounted for ~ 88-91 % in the energy budget, lower values were measured for warmer (marine) clouds during flight AC19. As shown in Section 4.1, S_v has a strong linear dependence on temperature, since this supersaturation component is associated with the W_s term. These results show that in warmer environments, a larger amount of energy relative to Q is expended for the air parcel's expansion, leading to a smaller decrease in the cloud parcel's internal energy and a lower cooling rate.

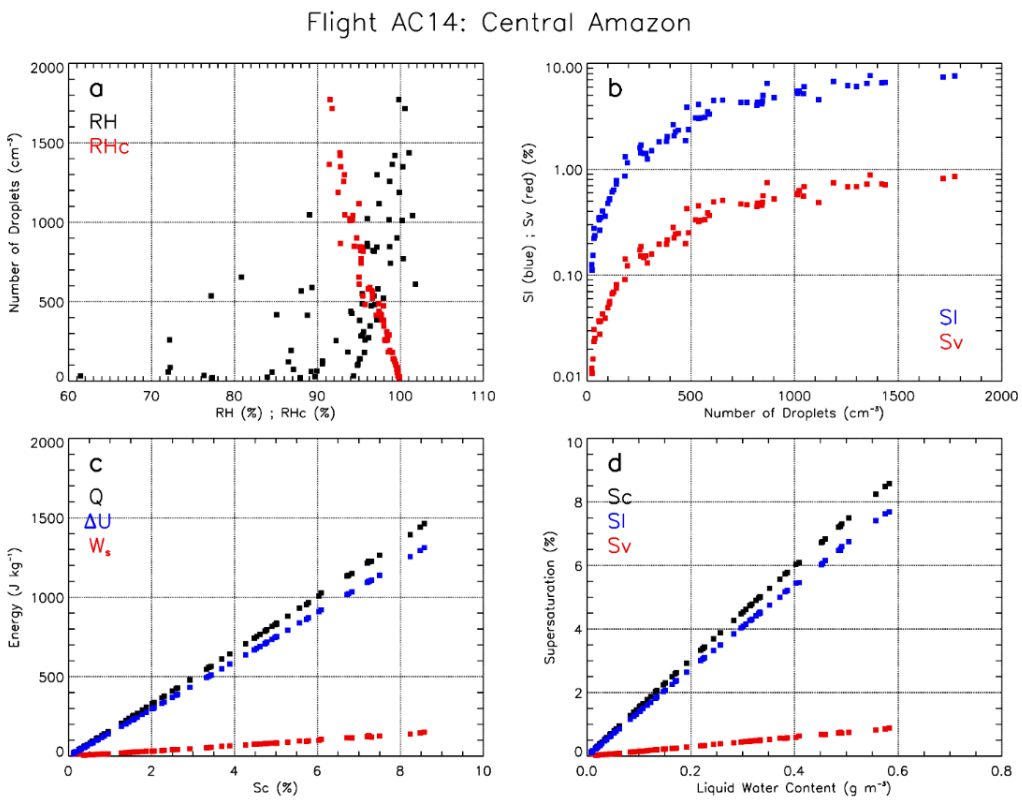

Figure 4. Cloud microphysical and thermodynamic properties measured at cloud bases of growing convective cumuli during Flight AC14. (a) RH versus N_d (black) and RH_c versus N_d (red). (b) N_d versus S_l (blue) and N_d versus S_v (red). (c) S_c versus Q, $|\Delta U|$, and W_s. (d) *LWC* versus S_c, S_l, and S_v.

Figure 5 shows the droplet number spectra as a function of cloud supersaturations (S_c, S_l, S_v), $N_d(S)$, derived from cloud base measurements for all flight segments (see Tables 3-5 for the statistics of the fit parameters). The $N_d(S)$ were derived using power-law fits of the form $N_d = C \cdot S^k$, where C is a scaling factor and k is the spectral exponent. Across all three supersaturations derived larger values of C and k parameters are estimated for aerosol-rich conditions (e.g., AC07), whereas smaller C and k values (e.g., AC19) reflect more CCN-limited regimes. The values of C and k have closer values for the power-law fits of N_d-S_c and N_d-S_l due to the similar values of Q and ΔU in the energetic budget partition ($\Delta U \sim 0.9 \cdot Q$). The high coefficients of determination ($R^2 > 0.87$) and low root-mean-square errors (RMSE < 0.3) indicate robust agreement between the fitted relationships and the observations under different atmospheric conditions. The tables show that the values of R^2 are sensitive to sample size, and larger cloud base datasets typically result in lower R^2 values due to the inclusion of a broader range of atmospheric variability. In our observations, larger samples encompass more heterogeneous conditions in updraft velocity, turbulence intensity, and CCN concentrations, which increase scatter in the N_d-S relationships. Nevertheless, the fitted parameters C and k remain relatively stable across the different environmental conditions owing to the underlying physical dependence between N_d and S. A more detailed description of this analysis accounting for different cloud detection thresholds and measurements uncertainties is provided in Section S2.3 of the Supplementary Material.

The $N_d(S_v)$ spectra calculated from the energetic budget analysis at cloud base are comparable to the $N_{CCN}(S_v)$ spectra observed near the surface level over marine regions and the Amazon Basin during the dry season (Khain and Pinsky, 2018; Pöhlker et al., 2016). Under clean marine conditions (flight AC19), the estimated N_d expected to activate at cloud base is about 740 cm^{-3} at S_v = 1 %. The maximum estimated S_v derived from the measurements is 0.27 %, corresponding to an adiabatic cooling (ΔT_c) of ~ 0.4 °C resulting from the closure analysis. In contrast, measurements obtained under more polluted conditions over forested regions during flights AC09 and AC18 show N_d values roughly twice as large for the same S_v. The maximum estimated S_v values derived from measurements were 0.34 % (ΔT_c = 0.53 °C) and 0.44 % (ΔT_c = 0.71 °C) for flights AC09 and AC18, respectively. Even larger N_d (S_v = 1 %) values are estimated for the data over the Central Amazon and the deforestation arc, where the droplet concentrations were more strongly influenced by emissions from urban activities and biomass burning. The largest estimated S_v value derived from the measurements (1.15 %) was calculated for flight leg AC17a corresponding to a ΔT_c of 1.81 °C.

The cloud properties observed under CCN-limited regimes were generally associated with regions of weaker buoyant forcing, resulting in lower LWC and weaker w, with maximum values ~ 2 m s^{-1} (Figure S19). In contrast, aerosol-rich environments were associated with stronger buoyant forcing and enhanced adiabatic cooling at cloud base, leading to larger LWC, higher S_v, and stronger w (up to ~ 4 m s^{-1}). Enhanced buoyant forcing also increased the variability of cloud-base measurements by strengthening fluctuations in the thermodynamic state of the cloud parcel (LWC, T, and p), which are the primary variables used in the energy budget and supersaturation calculations. However, the uncertainties in S_v do not scale directly with buoyant forcing itself, but rather with the uncertainty in these thermodynamic and microphysical measurements

(see Section S2.2). Consequently, the largest observed S_v and w values were generally associated with larger cloud base LWC values, consistent with stronger adiabatic cooling and enhanced condensational growth.

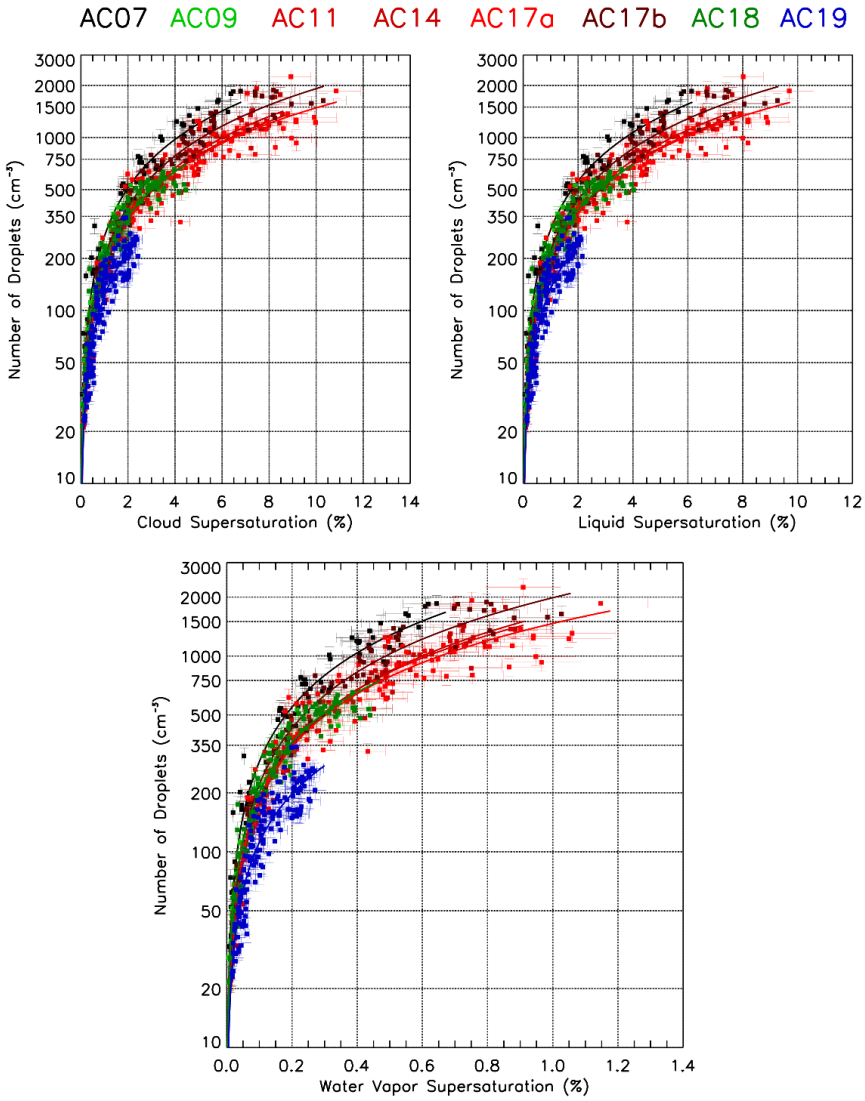

Figure 5. [upper-left] S_c vs. N_d for multiple flight segments (AC07, AC09, AC11, AC14, AC17a, AC17b, AC18, and AC19). Colored markers represent in-situ measurements, while solid curves correspond to power-law fits of the form $N_d = C \cdot S_c^k$. The colored markers correspond to different aerosol backgrounds in the Amazon region (red: Central Amazon, green: Northwestern Amazon, blue: Atlantic Ocean). [upper-right] and [bottom] Similar for S_l vs. N_d and S_v vs. N_d, respectively. Error bars indicate the uncertainties of N_d (10 %), S_c (~ 9.5 %), S_l (~ 9.2 %) and S_v (~ 12.6 %). The statistics of the power-law fits are presented in Tables 3, 4 and 5.

Table 3. Power-law fit parameters for the relationship $N_d = C \cdot S_v^{\,k}$ derived from log-log regression for each flight leg. The coefficients C and k are reported as Monte Carlo means ± 1σ (Nr = 5000 realizations). The coefficient of determination (R^2) and root-mean-square error (RMSE) are calculated from the nominal fit in logarithmic space. The uncertainties of N_d and S_v assumed in the calculations are 10 % and 12.6 %, respectively. Columns list: Flight leg, C, σC, k, σ k, R^2, RMSE, and sample size (N).

Flight	C	σC	k	σk	R^2	RMSE	N
AC07	2417.38	80.01	0.923	0.014	0.958	0.249	77
AC09	1352.97	83.48	0.828	0.022	0.952	0.19	41
AC11	1567.29	66.16	0.925	0.027	0.982	0.125	33
AC14	1644.66	51.57	0.974	0.015	0.981	0.164	73
AC17a	1467.06	33.21	0.904	0.012	0.947	0.26	121
AC17b	1985.79	63.35	0.955	0.018	0.975	0.161	64
AC18	1420.38	50.03	0.847	0.015	0.94	0.213	99
AC19	743.72	27.24	0.824	0.015	0.874	0.24	163

Table 4. Similar to Table 3 for power-law fit parameters for the relationship $N_d = C \cdot S_l^{\,k}$ derived from log-log regression. The uncertainties of N_d and S_l assumed in the calculations are 10 % and 9.2 %, respectively.

Flight	C	σC	k	σk	R^2	RMSE	N
AC07	294.68	5.18	0.929	0.014	0.958	0.249	77
AC09	224.36	5.47	0.832	0.022	0.953	0.188	41
AC11	188.26	7.58	0.953	0.028	0.983	0.12	33
AC14	187.47	3.87	0.989	0.016	0.983	0.157	73
AC17a	194.28	3.13	0.924	0.012	0.951	0.251	121
AC17b	224.05	5.82	0.973	0.019	0.977	0.153	64
AC18	210.78	3.17	0.856	0.015	0.942	0.209	99
AC19	133.77	1.57	0.832	0.015	0.876	0.238	163

Table 5. Similar to Table 3 for power-law fit parameters for the relationship $N_d = C \cdot S_c^{\,k}$ derived from log–log regression. The uncertainties of N_d and S_c assumed in the calculations are 10 % and 9.5 %, respectively.

Flight	*C*	σ*C*	*k*	σ*k*	R^2	RMSE	N
AC07	269.19	4.81	0.928	0.014	0.958	0.249	77
AC09	205.06	4.82	0.831	0.022	0.953	0.188	41
AC11	171.78	7.26	0.95	0.028	0.983	0.12	33
AC14	169.44	3.62	0.987	0.016	0.983	0.157	73
AC17a	176.91	2.96	0.922	0.012	0.95	0.252	121
AC17b	203.88	5.54	0.971	0.019	0.977	0.153	64
AC18	193.53	2.97	0.855	0.015	0.942	0.209	99
AC19	121.32	1.37	0.831	0.015	0.876	0.238	163

4.3 *Comparison of N_d (S_v) spectra vs. N_{CCN} (S_v) spectra*

The comparison of N_d (S_v) spectra vs. N_{CCN} (S_v) spectra is performed for four flight segments in Central Amazon, AC11, AC14, AC17a, and AC17b. The N_d (S_v) spectra are interpreted as representative of the sub-cloud N_{CCN}(S_v) population that was activated into cloud droplets after buoyant ascent to cloud base. During flights AC14 and AC17, the N_{CCN} (S_v) measurements were performed about 700 m below cloud base altitude, while during flight AC11, they were performed about 1400 m below cloud base (Tables 1 and 2). Therefore, the comparison should be interpreted as a closure between nearby sub-cloud CCN populations and cloud base droplet activation rather than as a strict Lagrangian comparison of identical air parcels. This observational configuration is illustrated schematically in Fig.1a.

Figure 6 shows N_{CCN}(S_v) spectra measured with CCNa for S_v ranging from ~ 0.2 % to ~ 0.55 % (red marks), while N_{CCN}(S_v) from CCNb was measured with a fixed S_v at ~ 0.55 % (blue marks). The corresponding N_d (S_v) spectra and the power-law fit parameters for each flight segment are shown in black. The fixed-S_v measurements from CCNb illustrate the variability of sub-cloud CCN concentrations for each flight segment. For segments AC11, AC14 and AC17a, the differences between minimum and maximum N_{CCN}(S_v) exceeded 1300 cm^{-3}, whereas during AC17b this range remained below 700 cm^{-3}. The large variability in N_{CCN}(S_v) is associated with heterogeneous air masses influenced by pollution plumes from biomass-burning and urban emissions. Under these conditions, the typical monotonic increase of N_{CCN}(S_v) with increasing S_v is not consistently observed in the CCNa measurements. This effect of pollution plumes in CCNa measurements is clearly shown in the figure where larger concentrations were measured for smaller S_v. In the flight segment AC17b, where a smaller variability of N_{CCN}(S_v) is observed in the CCNb sampling, N_{CCN}(S_v) measurements from CCNa are more consistent with those observed in homogenous air masses.

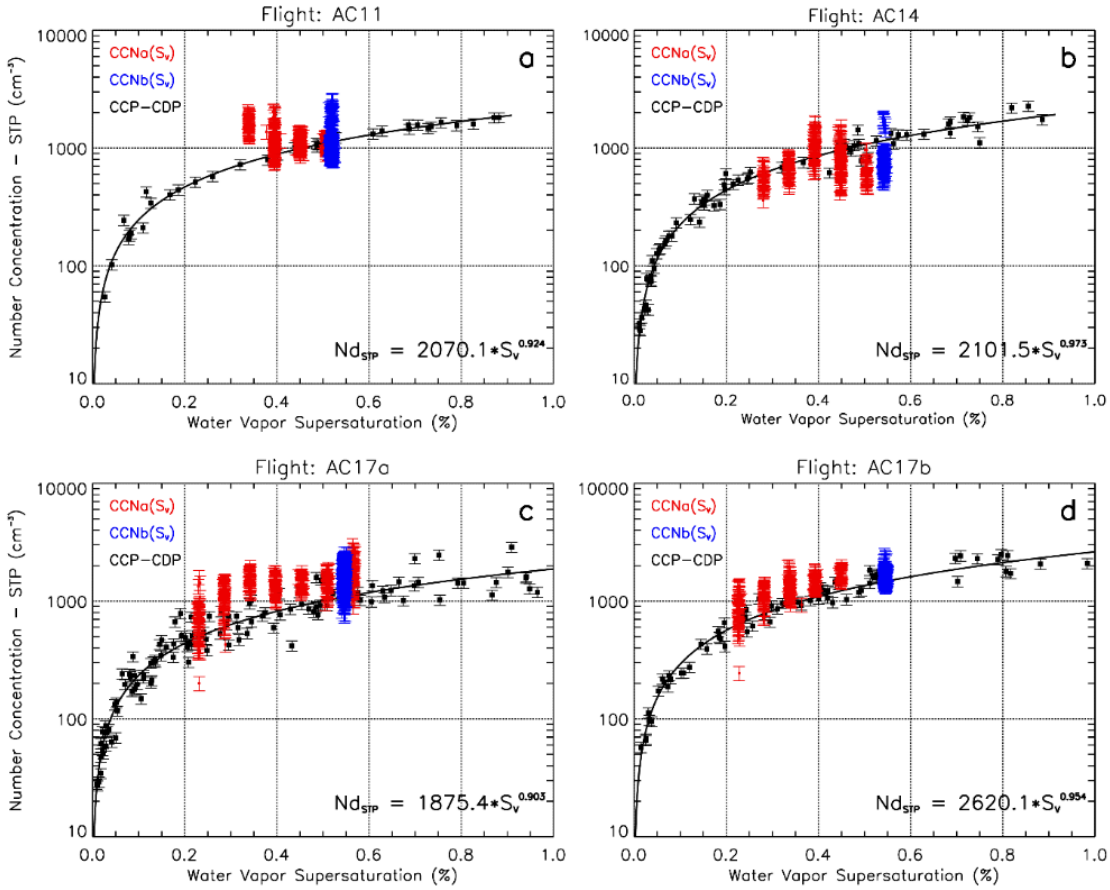

Figure 6. (a) S_v vs. N_d measured at cloud bases (black dots), and S_v vs. CCN concentrations measured below cloud bases (CCNa(S_v) in red and CCNb(S_v) in blue) during Flight AC11. N_d and CCN concentrations are calculated at standard temperature (0°C) and pressure (1013.25 hPa) (STP). Solid curves correspond to power-law fits of the form $N_d = C \cdot S_v^k$. (b), (c), and (d), similar data from flight legs AC14, AC17a, and AC17b, respectively. Error bars indicate the estimated uncertainties of N_d and CCN concentrations (10 %). Uncertainties of S_v from CCN counters (14 %) and theoretically derived (~ 12.6 %) are not shown for clarity.

Figure 7 shows the $N_d(S_v)$ spectra and the $N_{CCN}(S_v)$ measurements for time intervals during which both CCNa and CCNb were operating and the sampling duration exceeded 20 s (~ 1 km horizontal distance). The $N_{CCN}(S_v)$ measurements are displayed using the same color for each fixed-S_v cycle of the CCNa measurements. The measurements during Flight AC11 exhibit a clear influence of pollution plumes, with CCN concentrations reaching up to ~2000 cm^{-3} in both counters measuring in different S_v. Large concentration peaks are frequently observed in flight segment AC17a for a wide range of S_v measurements. Overall, most $N_d(S_v)$ and $N_{CCN}(S_v)$ values remain within the combined uncertainty bounds, whereas the largest deviations are associated with variability in polluted air masses and with derived $N_d(S_v)$ values from cloud passes

more strongly affected by the entrainment and mixing of dry air. The spatial and temporal heterogeneity of the sampled air masses during AC11, AC14, and AC17a also contributes to deviations in the fitted relationships over specific supersaturation ranges (e.g., near $S_v \approx 0.55$ % during AC14). Additional discrepancies between $N_d(S_v)$ and $N_{CCN}(S_v)$ concentrations may arise from differences in the particle diameter (d) detection ranges of the CCP-CDP probe (approximately 3-50 µm) and the CCN counters (activated droplets with $d \gtrsim 1$ µm), since the CCN counters may detect activated particles that have not yet grown to the minimum detectable size of the CCP-CDP probe at cloud base.

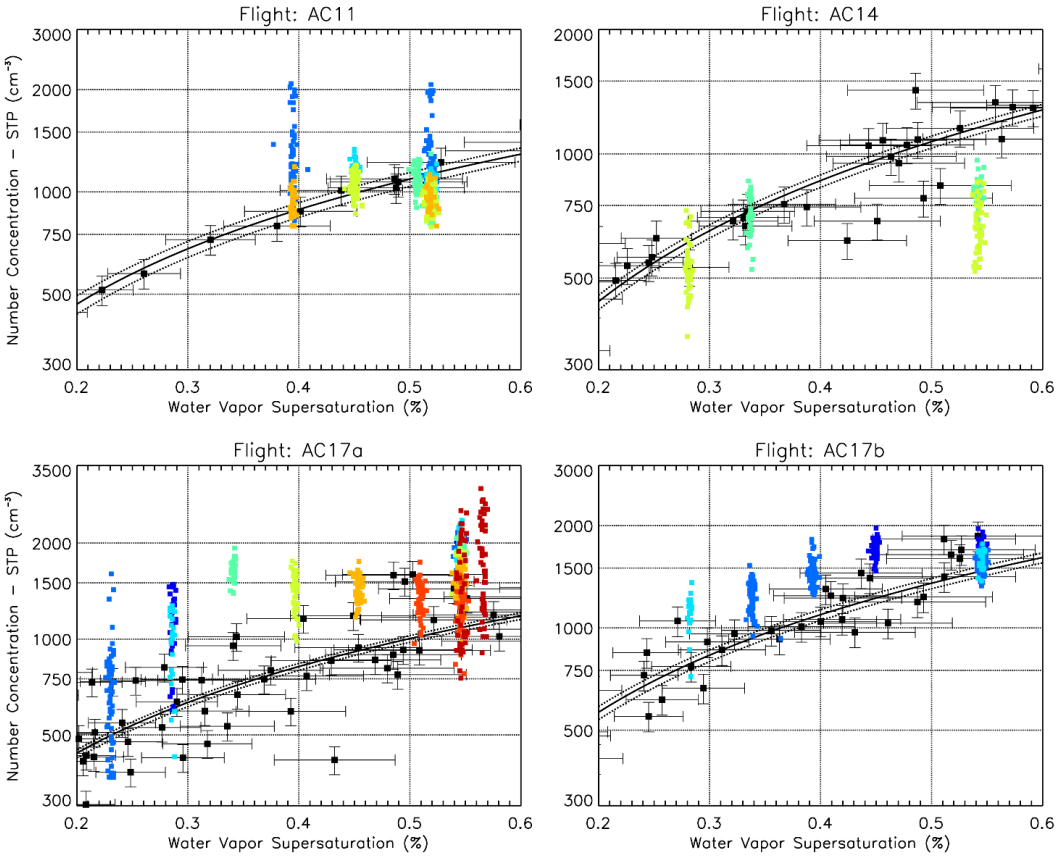

Figure 7. Relationship between cloud-base $N_d(S_v)$ spectra and sub-cloud $N_{CCN}(S_v)$ measurements at STP for flight segments AC11, AC14, AC17a, and AC17b over Central Amazon. Black symbols show the $N_d(S_v)$ observations at cloud base with the corresponding power-law fits, while colored symbols represent $N_{CCN}(S_v)$ measurements from CCNa and CCNb. The colored measurements are grouped according to individual CCNa supersaturation cycles with fixed S_v. Only periods with simultaneous operation of both CCN counters and sampling durations longer than 20 s (~ 1 km horizontal distance) are included. Error bars indicate the estimated uncertainties of N_d (10 %) and S_v (~ 12.6 %). Uncertainties of S_v from CCN counters (14 %) and in CCN concentrations (10 %) are not shown for clarity.

5 Conclusions

The thermodynamic framework introduced in this study provides a diagnostic estimate of water vapor supersaturation (S_v) at the base of warm cumulus clouds by treating the transition between saturated-vapor to vapor-liquid states as adiabatic and reversible under a local quasi-isobaric approximation. Airborne observations over the Central Amazon reveal that $N_d(S_v)$ spectra at cloud base agree within the uncertainty range of $N_{CCN}(S_v)$ spectra measured below cloud base, indicating that the water vapor pressure derived from the thermodynamic equations is physically consistent with that generated in CCN counters. In both cases, the water vapor pressure results from a thermal gradient under saturated conditions. In CCN counters, S_v is produced within a continuous-flow chamber by imposing controlled temperature gradients (warmer downstream) along wet walls. These gradients promote differential diffusion of water vapor and heat, leading to an enhanced water vapor pressure along the flow axis that exceeds saturation at the local air temperature. In the proposed diagnostic framework, S_v inferred from cloud base in-situ measurements represents the vapor-phase contribution to cloud supersaturation resulting from adiabatic cooling and is associated with the fraction of the latent energy partitioned into water-vapor expansion work (W_s) during the condensational growth.

The calculated $N_d(S_v)$ spectra at cloud base in different thermodynamic and aerosol conditions over the Amazon Basin and Atlantic Ocean have shown a typical variability expected at ground-based $N_{CCN}(S_v)$ spectra measured in clean and polluted conditions (Khain and Pinsky, 2018; Pöhlker et al., 2016). However, the methodology relies on several idealized assumptions - thermodynamic reversibility, negligible entrainment (adiabaticity), and accurate in situ microphysical and thermodynamic measurements - that may not fully capture the complexity of heterogeneous and highly turbulent cloud bases. Despite these assumptions, the diagnostic methodology adds new insights for the modeling of cloud base supersaturation and energetics, offering a physically consistent constraint on droplet activation and condensational growth. Under the assumption of conserved isobaric enthalpy at cloud base, the energy budget and cloud supersaturation components of the saturated parcel can be estimated from the temperature change during adiabatic cooling or, equivalently, from in situ measurements of liquid water content, which constrain the enthalpy change associated with the conversion of water vapor into liquid water. Within the proposed framework, neglecting the energetic cost of water vapor expansion assigns a larger fraction of the available energy to vapor-to-liquid conversion. This suggests a possible tendency to overestimate condensate production, latent heating, buoyancy and associated updraft velocities in simplified parcel calculations that do not explicitly account for this energetic partition.

Future studies applying energetic budget analyses to in situ measurements may extend this framework to estimate S_v at cloud base in other regions of the globe characterized by different aerosol and thermodynamic conditions. The method described in this manuscript is especially relevant when $N_{CCN}(S_v)$ measurements are unavailable. Furthermore, the thermodynamic evolution of cloudy parcels can be investigated within the context of the energetic budget to infer S_v from the vertical profiles of air temperature and dew-point temperature, with the parcel evolution physically interpreted in terms of dry- and cloud-adiabatic cooling. Such extensions would enable a more comprehensive quantification of the coupled microphysical

and energetic responses of clouds under diverse atmospheric conditions, including aerosol-cloud interactions, condensational droplet growth and evaporation.

Appendix A

The derivation of Eq. (1) can be found in cloud physics textbooks such as Rogers and Yau (1989) and Khain and Pinsky (2018), which describe the supersaturation tendency equation over water for an adiabatically ascending air parcel under the assumption of small water vapor supersaturation ($|S_v| \ll 1$):

$$\frac{dS_v}{dt} = A_1 \cdot w - A_2 \frac{dLWC}{dt} \qquad [s^{-1}] \qquad (A.1)$$

Where, A_1 and A_2 are given by:

$$A_1 = \frac{g}{T}\left(\frac{L_v}{c_{pd}R_vT} - \frac{1}{R_d}\right) \quad (A.2)$$

$$A_2 = \frac{1}{\rho_v} + \frac{{L_v}^2}{c_{pd}R_vT^2\rho_{air}} \quad (A.3)$$

The equations are derived from the thermodynamic equations governing temperature, water vapor mixing ratio, and the Clausius–Clapeyron relation. The coefficient A_1 represents the production of supersaturation during adiabatic parcel ascent, resulting from the differential changes in vapor pressure and saturation vapor pressure during adiabatic expansion, whereas A_2 represents the depletion of supersaturation during condensation; its first term accounts for the direct removal of water vapor, while its second term accounts for the increase in saturation vapor pressure caused by latent heat release. The derivation of A_1 is resulting from differentiating S_v, in the form $S_v = e/e_s - 1$, assuming parcel ascent with no condensation. The derivation of A_2 follows the same general framework but additionally accounts for the effects of condensation through vapor depletion and latent heat release (Rogers and Yau,1989).

Table A1. List of symbols, variables, and physical constants used in this study. Thermodynamic variables are expressed as specific quantities per unit mass of dry air. Uppercase notation is retained for consistency with the energetic framework. The corresponding extensive quantities are obtained by multiplying by the mass of dry air.

Symbol	Description	Units
RH	Relative Humidity	- or %
RH_c	Reference-state saturation ratio	- or %
RH_s	Saturation ratio at the reference state T_0	- or %
S	Supersaturation (general)	– or %
S_{QSS}	Quasi-steady supersaturation	%
S_c	Cloud Supersaturation	%
S_l	Liquid-phase Supersaturation	%
S_v	Vapor-phase Supersaturation	%
e	Water vapor pressure	Pa
e_s	Saturation water vapor pressure	Pa
T	Temperature of the saturated parcel	K
T_c	Air Temperature in Celsius	°C
T_{ws}	Temperature of the saturated parcel considering W_s	K
T_0	Initial saturated temperature at cloud base	K
T_{air}	Air temperature after energetic partition	K
T_Q	Latent-heat-equivalent temperature	K
ΔT	Adiabatic cooling magnitude	K or °C
ΔT_c	Adiabatic cooling magnitude from closure analysis	K or °C
ΔT_Q	Temperature change associated with latent heating	K
L_v	Latent heat of vaporization	J kg^{-1}
Q	Latent heat released by condensation	J kg^{-1}
δQ	Differential latent heat release	J kg^{-1}
dH	Enthalpy change	J kg^{-1}
ΔU	Change in internal energy	J kg^{-1}
W_s	Saturation work	J kg^{-1}
p	Pressure of the cloudy parcel	Pa
p_0	Reference pressure of the cloudy parcel	Pa
q_l	Liquid water mixing ratio	kg kg^{-1}
r_s	Saturation mixing ratio	kg kg^{-1}
ρ	Moist air density	kg m^{-3}
ρ_{air}	Dry air density	kg m^{-3}

α_v	Specific volume of water vapor	$m^3\ kg^{-1}$
c_{pd}	Specific heat of dry air at constant pressure	$J\ kg^{-1}\ K^{-1}$
c_{pv}	Specific heat of water vapor at constant pressure	$J\ kg^{-1}\ K^{-1}$
c_{pl}	Specific heat of liquid water at constant pressure	$J\ kg^{-1}\ K^{-1}$
$c_{p,cloud}$	Specific heat capacity of cloud air at constant pressure	$J\ kg^{-1}\ K^{-1}$
R_d	Gas constant for dry air	$J\ kg^{-1}\ K^{-1}$
R_v	Gas constant for water vapor	$J\ kg^{-1}\ K^{-1}$
A_1	Thermodynamic coefficient for supersaturation production	m^{-1}
A_2	Thermodynamic coefficient for condensational depletion	$m^3\ kg^{-1}$
P	Supersaturation production term	s^{-1}
C_d	Condensation depletion term	s^{-1}
N_d	Cloud droplet number concentration	cm^{-3}
LWC	Liquid Water Content	$kg\ m^{-3}$ (or $g\ m^{-3}$)
RWC	Rainwater Content	$g\ m^{-3}$
w	Vertical velocity / updraft velocity	$m\ s^{-1}$
z	Altitude	m
t	Time	s
CCN	Cloud Condensation Nuclei	-
N_{CCN}	Number concentration of *CCN*	cm^{-3}
CCNc	CCN counter	-
CCNa	CCN counter column A	-
CCNb	CCN counter column B	-
C	Scaling coefficient of power-law fit	cm^{-3}
k	Exponent of power-law fit	-
κ	Particle hygroscopicity	-
RMSE	Root mean square error	-
σC	Uncertainty of coefficient C	-
σk	Uncertainty of exponent k	-
Nr	Number of Monte Carlo realizations	-
N	Sample size	-
R^2	Coefficient of determination	-
CCP	Cloud Combination Probe	-
CDP	Cloud Droplet Probe	-
CIPgs	Cloud Imaging Probe grayscale	-
CAS-DPOL	Cloud and Aerosol Spectrometer with depolarization	-
SHARC	Sophisticated Hygrometer for Atmospheric Research	-

HASI	HALO aerosol submicron inlet	-
HALO-CVI	HALO counterflow virtual impactor	-
STP	Standard temperature and pressure	-

Data availability

The ACRIDICON-CHUVA HALO aircraft data are available from the HALO database: https://halo-db.pa.op.dlr.de/mission/5. Derived quantities used in this analysis are available from the corresponding author upon reasonable request.

Author contributions

Conceptualization: RCB.
Formal analysis: RCB.
Methodology: RCB.
Investigation: RCB.
Visualization: RCB, RA.
Supervision: DH.
Writing—original draft: RCB, DH.
Writing—review & editing: RCB, DH, MW and RA.

Competing interests

The authors declare they have no competing interests.

Acknowledgements

We thank the Reef Restoration and Adaptation Program (RRAP) and Southern Cross University. We are further grateful for funding of project grant no. **316646266** by the Deutsche Forschungsgemeinschaft (DFG, German Research Foundation) within the framework of Priority Programme **SPP 1294** to promote research with HALO. We acknowledge FAPESP (São Paulo Research Foundation) projects 2009/15235-8, 2014/08615-7, 2022/13257-9, 2023/04358-9 and 2025/10608-3.

Financial support

This work was funded by the The Reef Restoration and Adaptation Program a partnership between the Australian Government's Reef Trust and the Great Barrier Reef Foundation.

References

Baumgardner, D., Abel, S. J., Axisa, D., Cotton, R., Crosier, J., Field, P., Gurganus, C., Heymsfield, A., Korolev, A., Krämer, M., Lawson, P., McFarquhar, G., Ulanowski, Z., and Um, J.: Cloud Ice Properties: In Situ Measurement Challenges, Meteorological Monographs, 58, https://doi.org/10.1175/amsmonographs-d-16-0011.1, 2017.

Bolton, D.: The computation of equivalent potential temperature., Mon. Weather Rev., 108, https://doi.org/10.1175/1520-0493(1980)108<1046:TCOEPT>2.0.CO;2, 1980.

Braga, R. C., Rosenfeld, D., Weigel, R., Jurkat, T., Andreae, M. O., Wendisch, M., Pöhlker, M. L., Klimach, T., Pöschl, U., Pöhlker, C., Voigt, C., Mahnke, C., Borrmann, S., Albrecht, R. I., Molleker, S., Vila, D. A., Machado, L. A. T., and Artaxo, P.: Comparing parameterized versus measured microphysical properties of tropical convective cloud bases during the ACRIDICON-CHUVA campaign, Atmos. Chem. Phys., https://doi.org/doi.org/10.5194/acp-2016-872, 2017a.

Braga, R. C., Rosenfeld, D., Weigel, R., Jurkat, T., Andreae, M. O., Wendisch, M., Pöschl, U., Voigt, C., Mahnke, C., Borrmann, S., Albrecht, R. I., Molleker, S., Vila, D. A., Machado, L. A. T., and Grulich, L.: Further evidence for CCN aerosol concentrations determining the height of warm rain and ice initiation in convective clouds over the Amazon basin, Atmos. Chem. Phys., 17, 14433–14456, https://doi.org/10.5194/acp-17-14433-2017, 2017b.

Braga, R. C., Ervens, B., Rosenfeld, D., Andreae, M. O., Förster, J.-D., Fütterer, D., Hernández Pardo, L., Holanda, B. A., Jurkat-Witschas, T., Krüger, O. O., Lauer, O., Machado, L. A. T., Pöhlker, C., Sauer, D., Voigt, C., Walser, A., Wendisch, M., Pöschl, U., and Pöhlker, M. L.: Cloud droplet formation at the base of tropical convective clouds: closure between modeling and measurement results of ACRIDICON–CHUVA, Atmos. Chem. Phys., 21, 17513–17528, https://doi.org/10.5194/acp-21-17513-2021, 2021a.

Braga, R. C., Rosenfeld, D., Krüger, O. O., Ervens, B., Holanda, B. A., Wendisch, M., Krisna, T., Pöschl, U., Andreae, M. O., Voigt, C., and Pöhlker, M. L.: Linear relationship between effective radius and precipitation water content near the top of convective clouds: measurement results from ACRIDICON–CHUVA campaign, Atmos. Chem. Phys., 21, 14079–14088, https://doi.org/10.5194/acp-21-14079-2021, 2021b.

Campos Braga, R., Rosenfeld, D., Weigel, R., Jurkat, T., Andreae, M. O., Wendisch, M., Pöhlker, M. L., Klimach, T., Pöschl, U., Pöhlker, C., Voigt, C., Mahnke, C., Borrmann, S., Albrecht, R. I., Molleker, S., Vila, D. A., Machado, L. A. T., and Artaxo, P.: Comparing parameterized versus measured microphysical properties of tropical convective cloud bases during the ACRIDICON-CHUVA campaign, Atmos. Chem. Phys., 17, 7365–7386, https://doi.org/10.5194/acp-17-7365-2017, 2017.

Ervens, B., Cubison, M. J., Andrews, E., Feingold, G., Ogren, J. A., Jimenez, J. L., Quinn, P. K., Bates, T. S., Wang, J., Zhang, Q., Coe, H., Flynn, M., and Allan, J. D.: CCN predictions using simplified assumptions of organic aerosol composition and mixing state: A synthesis from six different locations, Atmos. Chem. Phys., 10, 4795–4807, https://doi.org/10.5194/acp-10-4795-2010, 2010.

Feingold, G. and Heymsfield, A. J.: Parameterizations of condensational growth of droplets for use in general circulation models, J. Atmos. Sci., 49, 2325–2342, https://doi.org/10.1175/1520-0469(1992)049<2325:POCGOD>2.0.CO;2, 1992.

Ghan, S. J., Abdul-Razzak, H., Nenes, A., Ming, Y., Liu, X., Ovchinnikov, M., Shipway, B., Meskhidze, N., Xu, J., and Shi, X.: Droplet nucleation: Physically-based parameterizations and comparative evaluation, J. Adv. Model. Earth Syst., 3, https://doi.org/10.1029/2011ms000074, 2011.

Joint Committee for Guides in Metrology: Evaluation of measurement data — Supplement 1 to the "Guide to the expression of uncertainty in measurement" — Propagation of distributions using a Monte Carlo method, Evaluation, JCGM 101:2, 2008.

Kaufmann, S., Voigt, C., Heller, R., Jurkat-Witschas, T., Krämer, M., Rolf, C., Zöger, M., Giez, A., Buchholz, B., Ebert, V., Thornberry, T., and Schumann, U.: Intercomparison of midlatitude tropospheric and lower-stratospheric water vapor measurements and comparison to ECMWF humidity data, Atmos. Chem. Phys., 18, https://doi.org/10.5194/acp-18-16729-2018, 2018.

Khain, A. P. and Pinsky, M.: Physical Processes in Clouds and Cloud Modeling, https://doi.org/10.1017/9781139049481, 2018.

Khain, A. P., Beheng, K. D., Heymsfield, A., Korolev, A., Krichak, S. O., Levin, Z., Pinsky, M., Phillips, V., Prabhakaran, T., Teller, A., Van Den Heever, S. C., and Yano, J. I.: Representation of microphysical processes in cloud-resolving models: Spectral (bin) microphysics versus bulk parameterization, https://doi.org/10.1002/2014RG000468, 2015.

Kleinheins, J., Shardt, N., Lohmann, U., and Marcolli, C.: The surface tension and cloud condensation nuclei (CCN) activation of sea spray aerosol particles, Atmos. Chem. Phys., 25, https://doi.org/10.5194/acp-25-881-2025, 2025.

Köhler, H.: The nucleus in and the growth of hygroscopic droplets, Transactions of the Faraday Society, 32, 1152–1161, 1936.

Konwar, M., Maheskumar, R. S., Kulkarni, J. R., Freud, E., Goswami, B. N., and Rosenfeld, D.: Aerosol control on depth of warm rain in convective clouds, Journal of Geophysical Research Atmospheres, 117, 1–10, https://doi.org/10.1029/2012JD017585,2012, 2012.

Korolev, A. V. and Mazin, I. P.: Supersaturation of Water Vapor in Clouds, J. Atmos. Sci., 60, 2957–2974, https://doi.org/10.1175/1520-0469(2003)060<2957:SOWVIC>2.0.CO;2, 2003.

Kulkarni, G., Mei, F., Shilling, J. E., Wang, J., Reveggino, R. P., Flynn, C., Zelenyuk, A., and Fast, J.: Cloud Condensation Nuclei Closure Study Using Airborne Measurements Over the Southern Great Plains, Journal of Geophysical Research: Atmospheres, 128, https://doi.org/10.1029/2022JD037964, 2023.

Lance, S.: Coincidence errors in a cloud droplet probe (CDP) and a cloud and aerosol spectrometer (CAS), and the improved performance of a modified CDP, J. Atmos. Ocean. Technol., 29, 1532–1541, https://doi.org/10.1175/JTECH-D-11-00208.1, 2012.

Mallaun, C., Giez, A., and Baumann, R.: Calibration of 3-D wind measurements on a single-engine research aircraft, Atmos. Meas. Tech., 8, 3177–3196, https://doi.org/10.5194/amt-8-3177-2015, 2015.

[Masson-Delmotte, V., Zhai, P., Pirani, A., Connors, S. L., Péan, C., Berger, S., Caud, N., Chen, Y., Goldfarb, L., Gomis, M. I., Huang, M., Leitzell, K., Lonnoy, E., Matthews, J. B. R., Maycock, T. K., Waterfield, T., Yelekçi, O., Yu, R., Zhou, B., and (eds.): IPCC, 2021: Climate Change 2021: The Physical Science Basis, Cambridge University Press. In Press., 2021.

Namdari, S., Dmitrovic, S., Chen, G., Choi, Y., Crosbie, E., Digangi, J. P., Diskin, G. S., Ferrare, R. A., Hair, J. W., Kirschler, S., Nowak, J. B., Thornhill, K. L., Voigt, C., Vömel, H., Zeng, X., and Sorooshian, A.: Intercomparison of wind speed, temperature, and humidity data between dropsondes and aircraft in situ measurements, Atmos. Meas. Tech., 18, https://doi.org/10.5194/amt-18-4325-2025, 2025.

Petters, M. D. and Kreidenweis, S. M.: A single parameter representation of hygroscopic growth and cloud\ncondensation nucleus activity, Atmos. Chem. Phys., 1961–1971, https://doi.org/10.5194/acp-7-1961-2007, 2007.

Pinsky, M., Khain, A., Mazin, I., and Korolev, A.: Analytical estimation of droplet concentration at cloud base, Journal of Geophysical Research Atmospheres, 117, 1–14, https://doi.org/10.1029/2012JD017753, 2012.

Pöhlker, M. L., Pöhlker, C., Ditas, F., Klimach, T., Hrabe de Angelis, I., Araújo, A., Brito, J., Carbone, S., Cheng, Y., Chi, X., Ditz, R., Gunthe, S. S., Kesselmeier, J., Könemann, T., Lavrič, J. V., Martin, S. T., Mikhailov, E., Moran-Zuloaga, D., Rose, D., Saturno, J., Su, H., Thalman, R., Walter, D., Wang, J., Wolff, S., Barbosa, H. M. J., Artaxo, P., Andreae, M. O., and Pöschl, U.: Long-term observations of cloud condensation nuclei in the Amazon rain forest – Part 1: Aerosol size distribution, hygroscopicity, and new model parametrizations for CCN prediction, Atmos. Chem. Phys., 16, 15709–15740, https://doi.org/10.5194/acp-16-15709-2016, 2016.

Pöhlker, M. L., Zhang, M., Campos Braga, R., Krüger, O. O., Pöschl, U., and Ervens, B.: Aitken mode particles as CCN in aerosol- And updraft-sensitive regimes of cloud droplet formation, Atmos. Chem. Phys., 21, https://doi.org/10.5194/acp-21-11723-2021, 2021.

Reutter, P., Su, H., Trentmann, J., Simmel, M., Rose, D., Gunthe, S. S., Wernli, H., Andreae, M. O., and Pöschl, U.: Aerosol- and updraft-limited regimes of cloud droplet formation: influence of particle number, size and hygroscopicity on the activation of cloud condensation nuclei (CCN), Atmos. Chem. Phys., 9, 7067–7080, https://doi.org/10.5194/acp-9-7067-2009, 2009.

Rissler, J., Swietlicki, E., Zhou, J., Roberts, G., Andreae, M. O., Gatti, L. V., and Artaxo, P.: Physical properties of the sub-micrometer aerosol over the Amazon rain forest during the wet-to-dry season transition – comparison of modeled and measured CCN concentrations, Atmospheric Chemistry and Physics Discussions, 4, 3159–3225, https://doi.org/10.5194/acpd-4-3159-2004, 2004.

Roberts, G. C. and Nenes, a.: A Continuous-Flow Streamwise Thermal-Gradient CCN Chamber for Atmospheric Measurements, Aerosol Science and Technology, 39, 206–221, https://doi.org/10.1080/027868290913988, 2005.

Rogers, R. R. and YAU, M. K.: A short course of cloud physics, Third edit., Library of Congress, Oxford, UK, 1989.

Romps, D. M., Latimer, K., Zhu, Q., Jurkat-Witschas, T., Mahnke, C., Prabhakaran, T., Weigel, R., and Wendisch, M.: Air pollution unable to intensify storms via warm-phase invigoration, Geophys. Res. Lett., 50, e2022GL100409, https://doi.org/10.1029/2022GL100409, 2023.

Romps, D. M.: A method for calculating reliable supersaturation reveals low values in tropical rainy-season clouds, J. Atmos. Sci., 82, 1517–1527, https://doi.org/10.1175/JAS-D-24-0265.1, 2025.

Rose, D., Gunthe, S. S., Mikhailov, E., Frank, G. P., Dusek, U., Andreae, M. O., and Pöschl, U.: Calibration and measurement uncertainties of a continuous-flow cloud condensation nuclei counter (DMT-CCNC): CCN activation of ammonium sulfate and sodium chloride aerosol particles in theory and experiment, Atmos. Chem. Phys., 8, 1153–1179, https://doi.org/10.5194/acp-8-1153-2008, 2008.

Rosenfeld, D., Liu, G., Yu, X., Zhu, Y., Dai, J., Xu, X., and Yue, Z.: High-resolution (375 m) cloud microstructure as seen from the NPP/VIIRS satellite imager, Atmos. Chem. Phys., 14, 2479–2496, https://doi.org/10.5194/acp-14-2479-2014, 2014.

Rosenfeld, D., Zheng, Y., Hashimshoni, E., Pöhlker, M. L., Jefferson, A., Pöhlker, C., Yu, X., Zhu, Y., Liu, G., Yue, Z., Fischman, B., Li, Z., Giguzin, D., Goren, T., Artaxo, P., Barbosa, H. M. J., Pöschl, U., and Andreae, M. O.: Satellite retrieval of cloud condensation nuclei concentrations by using clouds as CCN chambers, Proceedings of the National Academy of Sciences, 113, 5828–5834, https://doi.org/10.1073/pnas.1514044113, 2016.

Squires, P.: The growth of cloud drops by condensation. I. General characteristics, Aust. J. Chem., 5, https://doi.org/10.1071/CH9520059, 1952.

Stevens, B., Ament, F., Bony, S., Crewell, S., Ewald, F., Gross, S., Hansen, A., Hirsch, L., Jacob, M., Kölling, T., Konow, H., Mayer, B., Wendisch, M., Wirth, M., Wolf, K., Bakan, S., Bauer-Pfundstein, M., Brueck, M., Delanoë, J., Ehrlich, A., Farrell, D., Forde, M., Gödde, F., Grob, H., Hagen, M., Jäkel, E., Jansen, F., Klepp, C., Klingebiel, M., Mech, M., Peters, G., Rapp, M., Wing, A. A., and Zinner, T.: A high-altitude long-range aircraft configured as a cloud observatory: The NARVAL expeditions, Bull. Am. Meteorol. Soc., 100, 1061–1077, https://doi.org/10.1175/BAMS-D-18-0198.1, 2019.

Twomey, S.: The nuclei of natural cloud formation part II: The supersaturation in natural clouds and the variation of cloud droplet concentration, Geofisica Pura e Applicata, 43, 243–249, https://doi.org/10.1007/BF01993560, 1959.

Varghese, M. and Prabhakaran, T. V.: Reconciling observed and predicted droplet concentration at the Indian summer monsoon cloud base, Science of the Total Environment, 973, https://doi.org/10.1016/j.scitotenv.2025.179077, 2025.

Wang, J., Lee, Y. N., Daum, P. H., Jayne, J., and Alexander, M. L.: Effects of aerosol organics on cloud condensation nucleus (CCN) concentration and first indirect aerosol effect, Atmos. Chem. Phys., 8, 6325–6339, https://doi.org/10.5194/acp-8-6325-2008, 2008.

Wendisch, M., Pöschl, U., Andreae, M. O., Machado, L. A. T., Albrecht, R., Schlager, H., Rosenfeld, D., Martin, S. T., Abdelmonem, A., Afchine, A., Araùjo, A., Artaxo, P., Aufmhoff, H., Barbosa, H. M. J., Borrmann, S., Braga, R., Buchholz, B., Cecchini, M. A., Costa, A., Curtius, J., Dollner, M., Dorf, M., Dreiling, V., Ebert, V., Ehrlich, A., Ewald, F., Fisch, G., Fix, A., Frank, F., Fütterer, D., Heckl, C., Heidelberg, F., Hüneke, T., Jäkel, E., Järvinen, E., Jurkat, T., Kanter, S., Kästner, U., Kenntner, M., Kesselmeier, J., Klimach, T., Knecht, M., Kohl, R., Kölling, T., Krämer, M., Krüger, M., Krisna, T. C.,

Lavric, J. V., Longo, K., Mahnke, C., Manzi, A. O., Mayer, B., Mertes, S., Minikin, A., Molleker, S., Münch, S., Nillius, B., Pfeilsticker, K., Pöhlker, C., Roiger, A., Rose, D., Rosenow, D., Sauer, D., Schnaiter, M., Schneider, J., Schulz, C., de Souza, R. A. F., Spanu, A., Stock, P., Vila, D., Voigt, C., Walser, A., Walter, D., Weigel, R., Weinzierl, B., Werner, F., Yamasoe, M. A., Ziereis, H., Zinner, T., and Zöger, M.: The ACRIDICON-CHUVA campaign: Studying tropical deep convective clouds and precipitation over Amazonia using the new German research aircraft HALO, Bull. Am. Meteorol. Soc., 160128144638003, https://doi.org/10.1175/BAMS-D-14-00255.1, 2016.

Zheng, Y. and Rosenfeld, D.: Linear relation between convective cloud base height and updrafts and application to satellite retrievals, Geophys. Res. Lett., 42, 6485–6491, https://doi.org/10.1002/2015GL064809, 2015.